Smith College

Smith ScholarWorks

Astronomy: Faculty Publications

Astronomy

1-1-1995

# Three-Dimensional Fabry-Perot Imaging Spectroscopy of the Crab Nebula, Cassiopeia A, and Nova GK Persei

Stephen S. Lawrence
*University of Michigan, Ann Arbor*

Gordon M. MacAlpine
*University of Michigan, Ann Arbor*

Alan Uomoto
*Johns Hopkins University*

Bruce E. Woodgate
*NASA Goddard Space Flight Center*

Larry W. Brown
*NASA Goddard Space Flight Center*

*See next page for additional authors*

Follow this and additional works at: https://scholarworks.smith.edu/ast_facpubs

Part of the Astrophysics and Astronomy Commons

## Recommended Citation

Lawrence, Stephen S.; MacAlpine, Gordon M.; Uomoto, Alan; Woodgate, Bruce E.; Brown, Larry W.; Oliversen, Ronald J.; Lowenthal, James D.; and Liu, Charles, "Three-Dimensional Fabry-Perot Imaging Spectroscopy of the Crab Nebula, Cassiopeia A, and Nova GK Persei" (1995). Astronomy: Faculty Publications, Smith College, Northampton, MA.
https://scholarworks.smith.edu/ast_facpubs/69

This Article has been accepted for inclusion in Astronomy: Faculty Publications by an authorized administrator of Smith ScholarWorks. For more information, please contact scholarworks@smith.edu

## Authors

Stephen S. Lawrence, Gordon M. MacAlpine, Alan Uomoto, Bruce E. Woodgate, Larry W. Brown, Ronald J. Oliversen, James D. Lowenthal, and Charles Liu

This article is available at Smith ScholarWorks: https://scholarworks.smith.edu/ast_facpubs/69

1995AJ....109.2635L

THE ASTRONOMICAL JOURNAL VOLUME 109, NUMBER 6 JUNE 1995

# THREE-DIMENSIONAL FABRY–PEROT IMAGING SPECTROSCOPY OF THE CRAB NEBULA, CASSIOPEIA A, AND NOVA GK PERSEI[1]

STEPHEN S. LAWRENCE AND GORDON M. MACALPINE
Department of Astronomy, University of Michigan, Ann Arbor, Michigan 48109

ALAN UOMOTO
Department of Physics and Astronomy, The Johns Hopkins University, Baltimore, Maryland 21218

BRUCE E. WOODGATE, LARRY W. BROWN, AND RONALD J. OLIVERSEN
Goddard Space Flight Center, Greenbelt, Maryland 20771

JAMES D. LOWENTHAL
Lick Observatory, University of California, Santa Cruz, California 95064

CHARLES LIU
Department of Astronomy, University of Arizona, Tucson, Arizona 85721
*Received 1994 August 24; revised 1995 February 10*

## ABSTRACT

Three-dimensional spatial models of the line-emitting gas in the Crab Nebula, Cassiopeia A, and the nova remnant of GK Persei have been developed from imaging spectroscopy taken with the Goddard Fabry–Perot Imager mounted on the McGraw-Hill 1.3 m and Hiltner 2.4 m telescopes of the Michigan–Dartmouth–MIT Observatory. The spatial model of the Crab Nebula in [O III] λ5007 emission reveals the thin, annular morphology of the "high-helium torus," the association of this torus and other bright filament loops with north–south bipolar asymmetry of the remnant shell, the structure of the filamentary shell at the boundary with the inner synchrotron cavity, and holes in the distribution of the brightest filaments at the ends of the major optical axis. Images of the fast-moving knots in Cas A in [S II] λλ6716, 6731 emission extend deeper than previously published broadband images, providing a more complete view of the limb-brightened, spherical edge of the remnant. The bright northern arch is imaged as two continuous rings of material distinct in velocity space. The larger ring includes the most highly redshifted material detected in Cas A, and incorporates many of the newly formed [O III] knots. The most blueshifted material occurs in the patchy nebulosity in the southeastern region of the remnant, and a large velocity asymmetry is seen in the radial and spatial velocities of the most highly blueshifted and redshifted optical knots. The data cube for the quasi-stationary flocculi in Cas A in $H_\alpha$+[N II] λλ6548, 6583 emission reveals more diffuse nebulosity than previously detected and shows a distribution contained within an elliptical region on the sky which extends well beyond the spherical distribution of FMKs. Isophotes of GK Per in $H_\alpha$+[N II] λλ6548, 6583 emission demonstrate the "boxiness" of the remnant as projected on the sky, show a lack of emission in the northern "front" and eastern "central" portions of the nebula, suggest the presence of a bulge-like structure in the south–southeast, and may indicate recent strengthening of emission in the northeastern limb. © *1995 American Astronomical Society.*

## 1. INTRODUCTION

Investigations of the structures of nebulae have traditionally used conventional techniques: either direct imaging through broad- or narrow-band filters or spectroscopy through a small aperture or narrow slit. While powerful tools, these methods have drawbacks in the study of extended sources. Fixed filters have poor spectral resolution and may not be able to resolve closely spaced emission lines, particularly in objects with large internal velocity dispersion. The central wavelength and bandwidth of a filter are fixed and tuning methods (by tilting or temperature changes) have limited range. It is expensive to buy a set of filters with well-matched velocity sampling that is suited to study a large number of objects with different internal velocity dispersions. And once such a matched set is produced, it is difficult to expand the observing program to include other objects.

Spectroscopy offers user-defined spectral resolution, but at the cost of spatial sampling. To achieve high-velocity resolution with minimum spatial overlap, it is necessary to use a small aperture or narrow slit. For extended sources, this means that only a small fraction of the total surface area is sampled, and conclusions about the global properties of the object are biased by the selection of slit positions and orientations. For faint objects with large proper motions, it is challenging to assure exact repositioning of the aperture so com-

[1]Based in part on research carried out at the MDM Observatory, operated by the University of Michigan, Dartmouth College, and the Massachusetts Institute of Technology.



© American Astronomical Society • Provided by the NASA Astrophysics Data System

1995AJ....109.2635L



parison of studies with different apertures or widely separated epochs is hazardous.

The development of stable, gap scanning etalons and large-format CCD detectors allows imaging Fabry–Perot interferometers to solve many of these problems. Modern instruments provide moderate- to high-resolution spectroscopic data ($10^2 \lesssim R_\lambda \lesssim 10^6$) simultaneous over a several arcmin field of view (Atherton *et al.* 1981; Bland & Tully 1989). Tunability of both the width and center of the bandpass alleviates the need for a set of fixed filters matched to individual objects, and allows the observing program to be altered at the telescope. In particular, the same velocity bandpass can be sampled for all emission lines. Large areas of an extended object can be imaged, so precise aperture positioning is not a concern. Observations can be summed across a spectral width that exactly contains the entire emission-line flux from the object, minimizing the contribution from continuum sources (night sky, diffuse stellar background, extended synchrotron emission) and improving the detection limit for faint features.

In this paper we present results from Fabry–Perot imaging spectroscopy of the Crab Nebula, Cassiopeia A, and the remnant of Nova GK Persei. In addition to information extracted directly from the data cubes, the spatial and velocity information has been combined with the radial expansion to produce three-dimensional spatial models of their line emission. The instrumentation and observations are described in Sec. 2, and the data reduction steps and development of the models are outlined in Sec. 3. The results for the Crab Nebula are discussed in Sec. 4, for Cas A in Sec. 5, and for GK Per in Sec. 6, followed by a summary in Sec. 7.

## 2. OBSERVATIONS

All observations reported here were made with the Goddard Fabry–Perot Imager (GFPI) mounted on the telescopes of the Michigan–Dartmouth–MIT (MDM) Observatory. The GFPI uses gap scanning etalons manufactured by Queensgate Instruments, Ltd. The etalons are controlled by a feedback system of capacitors and piezoelectric drivers that maintain plate parallelism to the order of $\lambda/200$. The detector used for this work was a Tektronix 512×512 thinned CCD with 27 $\mu$m pixels and a read noise of 6 $e^-$ rms. The GFPI images only the central interference order onto the CCD, resulting in a nearly monochromatic field of view. The optical layout is shown in Fig. 1 of Caulet *et al.* (1992). Light from the telescope focal plane is collimated, passed through the etalon and a blocking filter, and then reimaged onto the CCD. The blocker is an interference filter of typically 100 Å bandwidth used to eliminate all but one of the orders transmitted by the etalon. The GFPI has relatively low resolvance ($200 \lesssim R_\lambda \lesssim 1500$) as compared with most other imaging Fabry–Perot systems in use; this makes it ideal for spectral scans of young supernova remnants (SNRs), where full sampling of the large-velocity dispersion can be achieved in one or two nights of observing.

A spectral scan of the Crab Nebula was obtained in [O III] λ5007 emission using the 1.3 m McGraw-Hill telescope at the MDM Observatory in December of 1989. The GFPI etalon provided a bandpass of 5.3 Å FWHM corresponding to a velocity width of 320 km s$^{-1}$. Individual images had exposure times of 300 s and were separated by a scan increment of 2.2 Å (130 km s$^{-1}$). Atmospheric conditions were very good and the seeing was measured at 2″.7. Spectral scans of Cas A and the remnant of nova GK Per were obtained using the 2.4 m Hiltner telescope at the MDM Observatory in November of 1991. The high-velocity "fast-moving knots" (FMKs) of Cas A were scanned in [S II] λλ6716, 6731 emission with a bandpass of 14.4 Å FWHM (640 km s$^{-1}$) and incremented in 12.0 Å (535 km s$^{-1}$) steps. Exposure times were 600 s and the seeing ranged from 1″.5 to 2″.5. The low-velocity "quasi-stationary flocculi" (QSFs) of Cas A were scanned in $H_\alpha$+[N II] λλ6548, 6583 emission with a bandpass of 5.3 Å FWHM (240 km s$^{-1}$) and spacing of 3.0 Å (140 km s$^{-1}$). The exposure times were 600 s and the seeing was typically measured at 2″.3. The GK Per field was also scanned in $H_\alpha$+[N II] λλ6548, 6583 emission with a bandpass of 5.3 Å FWHM (240 km s$^{-1}$) and incremental spacing of 3.0 Å (140 km s$^{-1}$). Exposure times were 300 s and seeing was measured at 2″.1. Atmospheric conditions were good during data acquisition, however, high humidity spoiled the final nights of the observing run and prevented complete velocity scans of the Cas A FMKs in [S II] λλ6716, 6731 and GK Per in [N II] λ6548. The instrumental configurations and etalon parameters for these four spectral scans are listed in Table 1.

TABLE 1. Summary of observations.

| | Crab Nebula | Cas A FMKs | Cas A QSFs | Nova GK Per |
|---|---|---|---|---|
| Dates of observation | Dec 4-5 1989 | Nov 9-12 1991 | Nov 8-9 1991 | Nov 7-9 1991 |
| Scan range (Å) | 4977–5038 | 6609–6861 | 6548–6600 | 6536–6612 |
| Scan center (Å) | 5007 | 6735 | 6574 | 6574 |
| Emission lines | [OIII] | [SII] | $H_\alpha$ + [NII] | $H_\alpha$ + [NII] |
| | | Instrument | | |
| Telescope aperture (m) | 1.32 | 2.36 | 2.36 | 2.36 |
| Cassegrain ratio | f/7.5 | f/7.5 | f/7.5 | f/7.5 |
| Camera lens, $f_{cam}$ (mm) | 200 | 135 | 135 | 200 |
| Output Beam | f/5.0 | f/3.375 | f/3.375 | f/5.0 |
| | | Detector | | |
| Image scale (″ pixel$^{-1}$) | 0.84 | 0.66 | 0.66 | 0.46 |
| Field of View (″) | 430×430 | 338×338 | 338×338 | 235×235 |
| Gain (e$^-$ ADU$^{-1}$) | 4.22 | 2.13 | 2.13 | 2.13 |
| Exposure (seconds) | 300 | 600 | 600 | 300 |
| | | Etalon[a] | | |
| QI serial | ET 50-834 | ET 50-835 | ET 50-835 | ET 50-835 |
| FSR, $\Delta\lambda$ (Å) | 124 | 385 | 159 | 159 |
| Finesse, $N_e$ | 23 | 26.7 | 30 | 30 |
| Order, $n$ | 40 | 17 | 41 | 41 |
| Etalon gap, $l$ ($\mu$m) | 10.1 | 5.88 | 13.6 | 13.6 |
| Airy Resolution, $\Lambda\lambda$ (Å) | 5.3 | 14.4 | 5.3 | 5.3 |
| Airy Resolution, $\Lambda v$ (km s$^{-1}$) | 320 | 640 | 240 | 240 |
| Resolvance, $R_\lambda$ | 945 | 468 | 1,240 | 1,240 |
| Scan increment, $\delta\lambda$ (Å) | 2.2 | 12.0 | 3.0 | 3.0 |
| Scan increment, $\delta v$ (km s$^{-1}$) | 130 | 535 | 140 | 140 |
| Airy curvature, $K_\lambda$ (Å pix$^{-2}$) | $4.56 \times 10^{-5}$ | $1.35 \times 10^{-4}$ | $1.31 \times 10^{-4}$ | $5.99 \times 10^{-5}$ |
| Crossover radius (pixels) | 220 | 298 | 151 | 224 |
| Crossover radius (″) | 184 | 197 | 100 | 103 |

Notes to TABLE 1.

[a]Wavelength-dependent parameters are calculated at the scan center listed above.

Throughout this paper we use the symbolic conventions for Fabry–Perot imaging spectroscopy described in Appendices A and B of Bland & Tully (1989). In particular, the original, unprocessed set of observations for the *scan* of an emission line is referred to as the $I'(x,y,z)$ observed data cube, the sets of fully reduced observations are called the $I(\alpha,\delta,\lambda)$ calibrated data cubes, and the spatial models are denoted as $I(X,Y,Z)$. In this notation $x$ and $y$ refer to pixel

© American Astronomical Society • Provided by the NASA Astrophysics Data System

1995AJ....109.2635L



coordinates, $z$ to the etalon scan coordinate, $\alpha$ and $\delta$ to equatorial coordinates, $\lambda$ to wavelength, $X$ and $Y$ to spatial coordinates northward and eastward from the center of the remnant, and $Z$ to the spatial coordinate along the line of sight to Earth.

## 3. DATA REDUCTION

Initial reductions of the $I'(x,y,z)$ observed data cubes followed standard procedures for CCD images, employing the data reduction routines within IRAF.[2] Bad columns and other chip defects were removed from individual frames within each data cube by interpolation across the affected areas. Each image was bias subtracted and edited for cosmic rays. Flatfielding was achieved using median twilight sky flats or uniform dome flats taken through the same blocking filter and etalon configurations. Regions of blank sky in each frame were sampled in order to subtract the background sky emission. For the Crab Nebula scan, where the line and continuum emission occupied a large fraction of the field of view, a constant sky background value was determined from regions near the edge of each image. For the Cas A and GK Per scans, stars and regions of extended nebular emission were masked and a low-order cubic spline was fitted to the remaining sky background using the IRAF task IMSURFIT. This second technique was particularly effective at removing the broad, low-intensity rings produced by the night sky emission lines of OH present in some of the Cas A and GK Per frames. The standard KPNO tables were used to correct each image for atmospheric extinction according to the airmass at the time of observation.

Ghost images of the brighter field stars appeared in the data as a result of internal reflections between the blocking filter and the etalon. However, since each filter produced its own unique pattern of reflections, these ghosts were readily identified and masked. The ghosting pattern was first determined from high signal images of the calibration standard stars, and ghost images in the data were confirmed though a comparison of images taken at the same etalon spacing through separate blocking filters.

Due to the transmission profile of the blocking filters, it was necessary to normalize the individual images within a scan to a common level. The reference image for each scan was selected to match the etalon spacing used to observe the calibration standard stars, and generally was the image most closely centered at the peak of the blocking filter transmission profile. For the Crab Nebula scan, normalization was achieved by assuming that stars within the field of view have constant flux across the narrow spectral range sampled. The instrumental magnitudes of seven bright stars were measured in each image, and the average multiplicative factor needed to shift these stars to their flux levels in the reference image was determined and applied. The accuracy of this normalization procedure was confirmed by the successful removal of the synchrotron continuum from all images by a single continuum image scaled to the reference image.

For the Cas A and GK Per scans, which spanned strong stellar absorption lines, normalization was accomplished by comparing the digital photometry of field stars with spectra of these same stars taken expressly for this calibration. The spectral data were obtained through light cirrus using the Mark III spectrograph on the 2.4 m Hiltner telescope at the MDM Observatory in January of 1993, and reduced using standard IRAF routines. Careful comparison of the spectra of standard stars taken throughout the night indicate that while the amount of extinction was variable, the dependence of the extinction on wavelength was stable, i.e., the flux calibration is uncertain by a constant factor that is independent of wavelength. Therefore the field star spectra have been flux calibrated *relatively* to a measured accuracy of 5%, but not *absolutely*. The measured bandpass of the Fabry–Perot was convolved with the spectra of these stars to produce a predicted instrumental magnitude. The ratios of measured to predicted instrumental magnitudes were used to calculate the normalization factor for each star, and these were averaged to produce a mean normalization factor for each image.

Absolute flux calibrations for all scans were derived from images of accepted standard stars obtained in the same etalon configurations and processed through identical reduction steps. High resolution, flux calibrated spectra of the standard stars (Massey *et al.* 1988) were convolved with the instrumental profile to produce the predicted magnitudes used to fix the zero point of the flux calibration. Combining the uncertainties from the relative spectral reduction, the digital photometry of the field and standard stars, and the calculation of the mean normalization factors, we estimate that our absolute flux calibrations are good to 15%.

For the Crab Nebula, continuous emission from field stars and the synchrotron emission were removed by scaling and subtracting a continuum frame taken at $\lambda \approx 6000$ Å, far from strong nebular line emission. For the Cas A and GK Per scans, where continuum frames were not available, stars were manually removed using mask images created by visual comparison across the scans, sampling many different velocity ranges. The data cubes were left in terms of observed fluxes, and no corrections were made for interstellar extinction as a function of wavelength across the scan. The latter effect is potentially significant for the Cas A [S II] $\lambda\lambda$ 6716, 6731 scan, which spans more than 250 Å.

The wavelength calibration necessary to transform from scan coordinate ($z$) to wavelength ($\lambda$) was obtained from observations of spectral lamps. These scans provided the dispersion constant and also a direct measurement of the etalon transmission profile. The GFPI has active thermal control that maintains the etalon and blocking filters at constant temperature to within 0.5 °C. Scans of the spectral lamps were taken several times during each night of observation to monitor small thermal drifts. These drifts were always much less than the FWHM of the bandpass, and a mean wavelength–etalon spacing relationship was derived for each night.

The wavelength peak of the bandpass shifts to shorter wavelengths with increasing radius from the optical axis. As a result, a fixed scan coordinate ($z$) translates into a para-

[2]The Image Reduction and Analysis Facility (IRAF) is distributed by the Association of Universities for Research in Astronomy, Inc., under contract to the National Science Foundation.

© American Astronomical Society • Provided by the NASA Astrophysics Data System

1995AJ....109.2635L



bolic surface in wavelength space (λ). The shape of this surface is determined by instrumental parameters and the wavelength of observation, and is defined as the Airy curvature (see the discussion in Bland & Tully 1989). For the configurations used in our observations, the curvature is large enough that the peak of the bandpass at the edges of the chip is shifted to shorter wavelengths than the peak of the bandpass at the center of the adjacent image in the scan. The Airy curvature and the crossover radius at which the phase shift is equal to the scan increment are given for each scan in Table 1. For certain applications it is desirable to have a set of images that are "flat" in wavelength space. In order to remove the Airy curvature and produce such a set of isowavelength images, a linear interpolation was applied between intensities of the original, curved images.

Image registration was accomplished by aligning field stars. The positional relationship between pixel location $(x,y)$ and equatorial coordinates $(\alpha,\delta)$ for each object was developed using published coordinate data. For the Crab Nebula, the coordinates and proper motions from Wyckoff & Murray (1977, hereafter referred to as WM) were used to obtain a solution with an estimated positional accuracy of $\pm 0\farcs2$. For Cas A, coordinate data were taken from the *HST Guide Star Catalog* and also from Kamper & van den Bergh (1976, hereafter referred to as KB76), while the Guide Star Catalog and data from Küstner (1921) were used for GK Per. The solutions for these remnants have estimated positional accuracies of $\pm 0\farcs5$.

At this stage, the original $I'(x,y,z)$ observed data cubes were fully processed to provide two versions of an $I(\alpha,\delta,\lambda)$ calibrated data cube for each scan. The first was derived from the interpolated isowavelength images, producing an array representing a cubic volume sampled by a stack of flat planes in wavelength space. The second was created by directly accounting for the Airy curvature of the original images, resulting in an array representing an irregular volume sampled by a stack of shallow parabolic surfaces in wavelength space. This second, *irregular* $I(\alpha,\delta,\lambda)$ cube retained the measured intensities of each original image, and did not suffer any loss of flux or spectral resolution that might arise from the interpolation procedure.

To create three-dimensional isophotes, we made the minimal assumptions necessary to transform the irregular $I(\alpha,\delta,\lambda)$ data cubes into mappings of intensity in physical $(X,Y,Z)$ space. The first step was to assume a distance to each of the objects, then transform from $(\alpha,\delta)$ coordinates on the sky to linear $(X,Y)$ space. The second step was to convert the wavelength coordinate (λ) to a radial velocity using the Doppler formula, and then to linear $(Z)$ space by adopting a value for the age of each remnant. We assumed that the expanding filaments have had constant radial velocity since the time of explosion, which is reasonable given that these remnants are all young. While the models do not account for decelerations caused by swept up circumstellar or interstellar material, or for accelerations in the case of the Crab Nebula (Trimble 1968, hereafter referred to as T68), they should be representative of the filament geometries. In addition, the models retain the basic property that they are a straightforward, linear rescaling of the original, irregular $I(\alpha,\delta,\lambda)$ data cubes.

TABLE 2. Summary of model parameters.

| | Crab Nebula | Cas A FMKs | Cas A QSFs | Nova GK Per |
|---|---|---|---|---|
| Distance, $d$ (pc) | 2000 | 2800 | 2800 | 470 |
| Age, $\Delta t$ (yr) | 935 | 334 | 334 | 90.7 |
| Rest wavelength, $\lambda_0$ (Å) | 5006.9 | 6723.6 | 6562.9 | 6562.9 |
| RA of origin, $\alpha_{1950.0}$ | $05^h31^m31\farcs34$ | $23^h21^m12\farcs0$ | $23^h21^m12\farcs0$ | $03^h27^m47\farcs5$ |
| Dec of origin, $\delta_{1950.0}$ | $21°58'54\farcs1$ | $58°32'24\farcs0$ | $58°32'24\farcs0$ | $43°44'03\farcs8$ |
| Trimmed field size ( ″) | 420×420 | 330×330 | 330×330 | 115×115 |
| Velocity range (km s$^{-1}$) | −1800–+1800 | −5100–+6100 | −700–+1700[a] | −1200–+2200[a] |
| Cube size (ly) | 13.3×13.3×11.4 | 14.6×14.6×12.5 | 14.6×14.6×2.7[a] | 0.86×0.86×1.0[a] |
| Binning in $X,Y$ (pixels) | 10×10 | 5×5 | 5×5 | 5×5 |
| Resolution in $X,Y$ ( ″) | 8.4 | 3.3 | 3.3 | 2.3 |
| Resolution in $X,Y$ (ly) | 0.27 | 0.15 | 0.15 | $1.7 \times 10^{-2}$ |
| Resolution in $Z$ (Å) | 4.4 | 24.0 | 6.0 | 6.0 |
| Resolution in $Z$ (km s$^{-1}$) | 260 | 1250 | 270 | 270 |
| Resolution in $Z$ (ly) | 0.81 | 1.4 | 0.30 | $8.2 \times 10^{-2}$ |
| Vel. uncertainty (km s$^{-1}$) | 100 | 760 | 120 | 130 |

Notes to TABLE 2.

[a]In reference to $H_\alpha$ emission only. See discussion in text.

The origin of the $I(X,Y,Z)$ data cube for each model is a point near the center of expansion of the relevant remnant within the zero velocity plane determined by the rest wavelength of the emission line. The data cubes were trimmed of blank sky to center the origin within the $X-Y$ plane, but no corrections were made for systemic radial velocities. In our models, the etalon bandpass function was not deconvolved from the spectral axis, so the velocity resolution along the $Z$ axis is moderate to poor. Due to the wings of the etalon transmission profile, emission features with high intensities appear broadened along the $Z$ dimension. The $X$ and $Y$ axes were binned to bring the resolution closer to that of the $Z$ axis, although the final resolutions are not actually matched. A compromise was sought between the loss of spatial information in the $X-Y$ plane and the marked improvement in the visual appearance of a three-dimensional isosurface displayed with similar structural scales along all axes.

The adopted ages and distances, and the resulting sizes, scales, and resolutions of the trimmed and binned models are listed in Table 2. The resolution in the $X-Y$ plane is given in terms of the size of the binning element, listed in units of arcsec and light years (ly). The resolution in $Z$ is set by twice the sampling interval, in the sense of the minimum separation two distinct emission line features would need in order to be resolved as separate peaks. The $Z$ resolution is listed in units of angstroms, km s$^{-1}$, and ly.

In referring to the radial velocities of particular features in the discussions below, we quote the location in velocity space of the peak of the emission profile as determined by Gaussian fits to spectra extracted from the irregular $I(\alpha,\delta,\lambda)$ data cubes. The uncertainties of our velocity fits were determined following the method of Gebhardt *et al.* (1994). Using the measured instrumental profile, CCD noise characteristics, and estimated normalization errors, 1000 model observations of a given input spectrum were generated and fitted with a Gaussian profile. The adopted velocity uncertainty is taken to be the biweight scale estimate (discussed in Beers *et al.* 1990) of the resulting distribution of fitted velocities, taken from the simulations of the faintest emission line features actually fit in each model. These velocity uncertainties are also given in Table 2.

The color images presented in the discussion section be-

© American Astronomical Society • Provided by the NASA Astrophysics Data System

1995AJ....109.2635L



low were created by using a Stardent 3000/750 Graphics Supercomputer and the Application Visualization System (AVS) software to render perspective views of three-dimensional surfaces of constant line intensity. The first step in generating these isosurfaces was to locate all volume elements (voxels) within a data cube that intersected the desired intensity level. Each voxel is a cubic volume defined by eight data points located at its corners, with each data point having an intensity and radial velocity associated with it. A voxel intersected the desired intensity level if at least one of the corner points had a higher intensity value and at least one had a lower intensity value. A three-dimensional interpolation was performed between the eight intensity values from the corners of each voxel in order to estimate the spatial location and radial velocity of a point with the desired intensity level within that voxel. Each of these interpolated points was then connected with those in adjacent voxels in order to trace out the desired isosurface as a "wire frame" composed of triangular facets. Each interpolated point was color coded according to its radial velocity, with blue representing velocity of approach and red representing velocity of recession. The wire-frame isosurface was then given a smooth, solid appearance by using a Gouraud shading algorithm to blend the colors of the interpolated points across the triangular facets. Once generated at a particular intensity level, the AVS program allowed the isosurface to be rotated and rendered in perspective from any viewing angle.

## 4. THE CRAB NEBULA

### *4.1 Background*

The Crab Nebula is the remnant of the supernova reported in A.D. 1054. It is one of the nearest and brightest of known SNRs, and its ~950 yr age and location ~200 pc below the galactic plane indicate that the supernova ejecta should be relatively uncontaminated from swept-up interstellar material. The ejecta are predominantly heated by synchrotron radiation from within the remnant, rather than shock heated; so physical conditions and element abundances in the gas can be analyzed through numerical photoionization models. A detailed understanding of the physical conditions, chemical composition, distribution, and kinematics of the filamentary gas should provide strong constraints on the mass and evolutionary state of the progenitor star, the processes of nucleosynthesis prior to and during the supernova event, and the role of the pulsar in the evolution of a plerion SNR.

Abundance analyses of individual positions within the nebula derived from spectroscopy and photoionization modeling have shown that helium is significantly overabundant relative to hydrogen overall, and that abundances can vary significantly in differing spatial locations. The abundance of nitrogen relative to carbon and oxygen is low and difficult to reconcile with the expectation that CNO processing should have occurred in a progenitor massive enough to produce a neutron star. The great strength of the nickel lines, especially relative to iron, is also a particularly vexing problem. The relative line intensities vary markedly with position in the remnant, and are correlated with large-scale filamentary structure, an understanding of which is important for abundance analyses. A detailed discussion of these problems, along with references to past spectroscopic, imaging and analytic studies, is presented in the review by Davidson & Fesen (1985).

A great deal of research has also been concerned with the kinematics and morphology of the remnant shell as a whole. Several of the recent studies have revealed a large-scale, north–south bipolar asymmetry in the abundance, geometry, and velocity distribution of the bright filaments. In particular, Uomoto & MacAlpine (1987) detected a "high-helium band" of filamentary gas stretching E–W on the plane of the sky, which they calculated to be $\gtrsim$90% helium by mass. Spectra running north–south across the face of the nebula taken by MacAlpine *et al.* (1989, hereafter referred to as M89) exhibit pinched velocity ellipses associated with the high-helium band, and they postulated that the structure is a complete torus that has constrained the expansion of the filamentary shell in the East–West plane and caused the North–South bipolar lobe structure. Studies of the polarization, proper motions, and morphology of the synchrotron nebulosity have provided further evidence for north–south axial phenomena. Michel *et al.* (1991) detected a N–S aligned hourglass pattern in linearly polarized optical synchrotron emission, which they interpreted in terms of a tightly wrapped magnetic torus surrounding the pulsar. Fesen *et al.* (1992) postulated the existence of a much larger magnetic torus responsible for the east and west bays in the synchrotron nebula, possibly arising from pre-SN mass loss in an E–W equatorial plane. Another well-studied phenomenon with a N–S axis is the "jet" first reported by van den Bergh (1970). This feature is a roughly $45'' \times 90''$ extension of the filamentary and synchrotron emission beyond the northern boundary of the remnant, with an appearance suggestive of a limb-brightened, hollow cylinder (see Fesen & Staker 1993 and references therein). The kinematics of filaments in the jet walls indicate that it is moving radially outward from the center of expansion and is tilted only a few degrees from the plane of the sky, very nearly perpendicular to the E–W structures described above. Filaments in the main body of the remnant located at the base of the jet also display the lowest helium abundances and strongest [Ni II] emissions detected in the nebula. Additionally, MacAlpine *et al.* (1994, hereafter referred to as M94) have recently reported the detection of a series of compact, line-emitting knots which are strikingly aligned to the north and south of the pulsar and demonstrate remarkably strong [Ar III] λλ 7136, 7751 emission. These "argoknots" were initially discovered during the course of the Fabry–Perot observations presented here.

### *4.2 Discussion*

The irregular $I(\alpha,\delta,\lambda)$ data cube for [O III] λ5007 line emission from the Crab Nebula was converted into $(X,Y,Z)$ linear space using a distance of 2,000 pc (Trimble 1973) and an age of 935 yr. As this distance was primarily derived from expansion parallax methods equating the maximum radial velocity with proper motions along the minor axis of the nebula, we expected *a priori* that our model would result in a prolate shape with its major axis roughly contained in the

© American Astronomical Society • Provided by the NASA Astrophysics Data System

1995AJ....109.2635L



plane of the sky. For convenience, the origin of the $X-Y$ plane was selected to be the location of the pulsar, calculated to be at $\alpha_{1950}=05^h31^m31^s.34$, $\delta_{1950}=21°58'54''.1$. Using data from WM, the location of the pulsar in 1989 was ~12″ WNW from its position at the time of the explosion in 1054 AD, so the chosen origin is close to the true center of expansion of the nebula. The trimmed 420″ square field of view subtends 13.3 ly; This includes the main body of the nebula and roughly half of van den Bergh's jet, which is faintly visible in our data. Individual images within the scan were binned in 10×10 pixel blocks, decreasing the $X$ and $Y$ resolution closer to that of the $Z$ axis and improving the appearance of the displayed isosurfaces. The resulting resolution in the plane of the sky is 0.27 ly. The scan covers 4977–5038 Å with an Airy resolution of 5.3 Å FWHM, which samples the nebula in a 3600 km s$^{-1}$ range centered on 5007 Å. The resolution in velocity space, as defined by twice the scan increment, corresponds to a spatial resolution of 0.81 ly along the $Z$ axis. The uncertainty in the velocities of fitted line peaks is 100 km s$^{-1}$. Further parameters of the spatial model are listed in Table 2.

Prior to the conversion to linear space, a correction was applied to remove highly redshifted [O III] λ4959 emission from the data cube. Using the theoretical emission ratio between λ4959 and λ5007 in the low-density limit, interpolated velocity slices from the highly redshifted end of the λ5007 scan were scaled and subtracted from the appropriate velocity slices in the blueshifted end.

Because of the coarse resolution in the spatial model, features referred to as "filaments" or "filament loops" in the discussion below do not necessarily represent physically contiguous structures, and may instead be large-scale alignments or clusters of smaller line-emitting features. Indeed, van den Bergh & Pritchet (1986) and Hester *et al.* (1994) have shown that many filaments that appear continuous under typical ground-based seeing conditions can be resolved into chains or groups of closely spaced knots with size scales down to 0″.5 or less. Our own data cubes reveal a tremendous amount of small-scale structure that is normally lost due to blending of features at different radial velocities by the wider bandpasses of conventional imaging techniques. In analyzing the large-scale morphology of the line-emitting gas displayed in our coarse spatial model, it is important to keep in mind that the structures may actually represent an integration over spatially clustered but much smaller-scale features which can span a variety of ionization, temperature, and density regimes. In the following discussion we refer to features using the broad coverage provided by the identifications from Table 2 and Plate I of Trimble (1970, hereafter referred to as T70), as well as the few, well-studied spectroscopic positions of Miller (1978), Fesen & Kirshner (1982, hereafter referred to as FK82), and Henry *et al.* (1984, hereafter referred to as HMK).

Four views of the isophotal model of the Crab in [O III] λ5007 emission are presented in Fig. 1 (Plate 82). The isophotal level was set to a large value, $6.0\times10^{-14}$ erg s$^{-1}$ cm$^{-2}$, to show the spatial orientations of only the very brightest [O III] emitting filaments. This allows for the clearest views of the entire nebular structure, as isophotes displaying lower intensity emission become too filled in to view the front and back sides simultaneously or to give a clear impression of individual filament geometries. Figure 1(a) displays the model viewed along the line of sight to the Earth, showing the front side of the remnant. North is up and east is to the left. Figure 1(b) presents the model viewed 180° from the vantage point of Fig. 1(a), showing the back side of the remnant. North is up and east is to the right. Figure 1(c) is a view 60° E from the line of sight to the Earth, and 30° S of the E–W plane. This is roughly equivalent to viewing the remnant from the southeast, sighting along the major optical axis. Figure 1(d) illustrates a line of sight 120° W and 30° S of the E–W plane, nearly orthogonal from that of Fig. 1(c). The color coding represents radial velocity with respect to the Earth; darkest blue is −1500 km s$^{-1}$, deepest red is +1400 km s$^{-1}$, and green is the zero radial velocity plane.

The interpolated $I(\alpha,\delta,\lambda)$ data cube is presented as a mosaic of frames in Fig. 2 (Plates 83 and 84). These frames represent the component images of the [O III] scan, taken at sequentially incremented wavelengths corresponding to 130 km s$^{-1}$ steps in velocity space. They have been reduced through flux calibration and continuum subtraction, and have been interpolated to remove the phase shift caused by the Airy curvature. All are oriented with north up and east to the left, and the central wavelengths of the bandpass for each frame are listed in Table 3. The figures display the majority of the [O III] scan, ranging from a radial velocity of −1430 (frame 1) to 0 km s$^{-1}$ (frame 12) in Fig. 2(a), and from +130

TABLE 3. Bandpass centers in Figs. 2, 4, 5, and 7.

| Frame | Fig. 2a Crab Nebula $\lambda_{cent}$[a] / $v_{cent}$[b] | Fig. 2b Crab Nebula $\lambda_{cent}$[a] / $v_{cent}$[b] | Fig. 4a Cas A FMKs $\lambda_{cent}$[a] / $v_{cent}$[c] | Fig. 4b Cas A FMKs $\lambda_{cent}$[a] / $v_{cent}$[c] | Fig. 5 Cas A QSFs $\lambda_{cent}$[a] / $v_{cent}$[d] | Fig. 7 Nova GK Per $\lambda_{cent}$[a] / $v_{cent}$[e] |
|---|---|---|---|---|---|---|
| 01 | 4982.9 | 5009.0 | 6610.7 | 6754.8 | 6560.6 | 6564.9 |
| | −1435 | +130 | −5035 | +1390 | −100 | −840 |
| 02 | 4985.1 | 5011.1 | 6622.7 | 6766.8 | 6563.4 | 6568.0 |
| | −1300 | +255 | −4500 | +1925 | +30 | −700 |
| 03 | 4987.3 | 5013.3 | 6634.7 | 6778.8 | 6566.3 | 6571.1 |
| | −1170 | +385 | −3965 | +2460 | +160 | −560 |
| 04 | 4989.4 | 5015.5 | 6646.7 | 6790.8 | 6569.1 | 6574.2 |
| | −1045 | +520 | −3430 | +2995 | +290 | −420 |
| 05 | 4991.6 | 5017.7 | 6658.7 | 6802.8 | 6572.0 | 6577.2 |
| | −915 | +650 | −2895 | +3530 | +420 | −280 |
| 06 | 4993.8 | 5019.8 | 6670.7 | 6814.9 | 6574.8 | 6580.3 |
| | −780 | +775 | −2360 | +4070 | +550 | −140 |
| 07 | 4995.9 | 5022.0 | 6682.7 | 6826.9 | 6577.7 | 6583.4 |
| | −655 | +910 | −1825 | +4605 | +680 | 0 |
| 08 | 4998.1 | 5024.2 | 6694.8 | 6838.9 | 6580.5 | 6586.5 |
| | −525 | +1040 | −1285 | +5140 | +810 | +140 |
| 09 | 5000.3 | 5026.3 | 6706.8 | 6850.9 | 6583.4 | 6589.5 |
| | −390 | +1165 | −750 | +5675 | +940 | +280 |
| 10 | 5002.5 | 5028.5 | 6718.8 | BLANK | 6586.3 | 6592.6 |
| | −260 | +1295 | −215 | | +1070 | +420 |
| 11 | 5004.6 | 5030.7 | 6730.8 | BLANK | 6589.1 | 6595.7 |
| | −135 | +1430 | +320 | | +1200 | +560 |
| 12 | 5006.8 | STACK | 6742.8 | STACK | STACK | 6598.8 |
| | −5 | | +855 | | | +700 |
| 13 | — | — | — | — | — | 6601.8 |
| | | | | | | +840 |
| 14 | — | — | — | — | — | 6604.9 |
| | | | | | | +980 |
| 15 | — | — | — | — | — | STACK |

Notes to TABLE 3.

[a]Wavelengths in units of Å.
[b]Velocity in km s$^{-1}$ relative to a rest wavelength of 5006.85 Å.
[c]Velocity in km s$^{-1}$ relative to a rest wavelength of 6723.60 Å.
[d]Velocity in km s$^{-1}$ relative to a rest wavelength of 6562.80 Å.
[e]Velocity in km s$^{-1}$ relative to a rest wavelength of 6583.39 Å.

© American Astronomical Society • Provided by the NASA Astrophysics Data System

1995AJ....109.2635L



(frame 1) to +1430 km s$^{-1}$ (frame 11) in Fig. 2(b). A stacked image formed by the addition of all images within the irregular $I(\alpha,\delta,\lambda)$ data cube is presented as frame 12 of Fig. 2(b). As indicated above, images in Fig. 2 have been processed to remove estimated contributions from highly redshifted [O III] λ4959 emission.

A number of noteworthy features can be seen in Figs. 1 and 2. The filament showing the most intense [O III] λ5007 emission and also the most contiguous extent in velocity is the formation that extends horizontally in the E–W plane in both Figs. 1(a) and 1(b). The blueshifted, front portion encompasses filaments 235, 236, 263, 264, 267–79, 277–80, 282–84, 299–301, 303–05, 333, 356, 357, 372, and 373 of T70, as well as Miller's position 2, positions 1 and 2 of FK82, and position 1 of HMK. The redshifted, rear portion includes filaments 273, 274, 354, and 355 of T70. This overall feature corresponds to the high-helium band or torus of Uomoto & MacAlpine (1987) and M89; and Figs. 1(a) and 1(b) confirm that it is indeed a torus, extending continuously from the regions of highly blueshifted emission [frame 1 of Fig. 2(a)] to those of highly redshifted emission [frame 9 of Fig. 2(b)] in the isophotal displays. The small break near the zero-velocity plane at the western edge of Fig. 1(a) is fully closed in displays at slightly lower intensity levels. Much of the emission from the entire torus comes from the thicker, blueshifted region slightly west of center in Fig. 1(a). The most intense emission within this region, also the point of greatest [O III] emission within the entire nebula, is roughly 50″ WSW of the pulsar with a radial velocity near −400 km s$^{-1}$ [frame 9 of Fig. 2(a)], situated between filaments 268 and 299 of T70. This feature is coincident with one of the regions of highest helium abundance found by Uomoto & MacAlpine (1987). From the sequence of frames in Figs. 2(a) and 2(b), the torus is seen to resemble a thin, annular sheet rather than a fat doughnut. For example, when viewed near the zero radial velocity plane [frame 12 of Fig. 2(a)], a cross-sectional slice through the eastern section of the torus does not have a circular appearance, but is significantly flattened and radially elongated (~8″ thick, ~60″ in radial extent). Measuring from local peaks in the [O III] emission, the torus extends across approximately 240″ on the sky and 2200 km s$^{-1}$ in velocity space, values which correspond in our model to diameters of 7.6 and 6.9 ly, respectively. Rescaling the $X,Y$ axes to place the nebula at a distance of 1800 pc results in a more circular torus of diameter 6.9 ly. Taking into account the difficulty of defining the plane of its warped circumference and the limited $Z$ axis resolution of the model, the torus appears fairly well centered near the pulsar in the zero radial velocity plane.

The rest of the bright [O III] filaments are arranged in a pattern that can best be described in relation to the the plane of the E–W torus. In Fig. 1(a) three major filamentary loops emerge nearly perpendicularly from the forward, blueshifted portion of the E–W torus. Two of these are connected with the torus near the region of highest emission, one extending north from filament 299 of T70 and the other to the south from filament 268 [frame 6 of Fig. 2(a)]. The third filament loop branches off northward from the torus somewhat east of the center in the region of filament 276 [frame 4 of Fig. 2(a)]. The blueshifted portion of the southern loop encompasses filaments 265, 266, 270, 340, 342, 343, and 351–53 of T70, as well as position 2 of HMK. Near the zero-velocity plane this loop splits into two separate features which can be seen in Fig. 1(b) to reconnect with the rearward, redshifted portion on the E–W torus [frames 4 through 6 of Fig. 2(b)]. The fainter, western, redshifted branch includes filaments 271, 272, 337, 338 of T70, and position 9 of FK82, while the brighter, eastern, redshifted branch encloses filaments 260–62, 287, 339, 341 of T70, Miller's position 1, and position 10 of FK82. The western filament loop that extends northward from filament 299 emerges from the E–W torus nearly perpendicularly, and then angles northeast as it approaches the zero velocity plane near the western base of the jet. It contains filaments 319–23, 325, 335, 358, 359 of T70 and position 7 of FK82 within the blueshifted portion of its length. Just before reaching the zero-velocity plane this loop also branches into two, which become fainter and broken, but run parallel to each other and reconnect with the E–W torus at high red-shift in Fig. 1(b). The brighter, eastern, redshifted branch of this loop includes filaments 314–17 and 324 of T70, as well as positions 5 and 6 of FK82. The fainter, western, redshifted branch is located mostly in projection behind the blueshifted portion of the loop, but appears to incorporate filaments 327–29, 364, and 365 of T70 and position 4 of HMK in its northern sections near the zero radial velocity plane. The eastern filament loop that leaves the E–W torus perpendicularly at filament 276 runs northward, crosses the zero velocity plane near the eastern base of the jet, then reconnects with the torus at an intermediate red-shift [shaded yellow in Fig. 1(b)]. This feature is traced in its northern regions by filaments 336, 367, and 368 of T70.

It is interesting to note that the brightest [O III] filaments described here appear to have a large-scale distribution connected with the E–W torus and the bipolar asymmetry of the nebula. The brightest filaments in the northern and southern portions of the remnant emerge from the torus nearly perpendicularly at negative radial velocities, are nearly parallel to our line of sight as they cross the zero radial velocity plane, and reconnect with the torus nearly perpendicularly at positive radial velocities. The strongest features in frame 12 of Fig. 2(a) are seen in their cross section, rather than along their lengths. The dynamical processes that created the N–S bipolar asymmetry seen in the abundance distributions and the velocity field also appear to have influenced the positions and alignments of these brightest filaments.

Our data cube confirms that most of the [O III] line-emitting gas is in a thick shell surrounding the central synchrotron cavity (T68; Chevalier & Gull 1975; Clark *et al.* 1983). This can be seen in Figs. 1(a) and 1(b), as all of the zero radial velocity gas is located at the periphery of the nebula. Line emission from the central regions is significantly Doppler shifted, and the emptiness of the central cavity persists even when the data cube is displayed at much lower isophotal levels. From an examination of frames 11 and 12 of Fig. 2(a) and frame 1 of Fig. 2(b), which bracket the zero radial velocity plane, the inner synchrotron cavity appears as an ellipse approximately 4.′0×2.′9 (7.5×5.4 ly) in extent, with a major axis position angle approximately 130°

© American Astronomical Society • Provided by the NASA Astrophysics Data System

1995AJ....109.2635L



E of N. The cavity is surrounded by a shell of filamentary emission that varies from 0.′6 to 1.′3 (1.0 to 2.5 ly) in thickness. The inner boundary of this shell is outlined by a thin (~3″–9″) layer of enhanced [O III] emission with short (~3″–15″), finger-like projections extending into the synchrotron cavity (see also the western sections of Fig. 1 of M94). These features are suggestive of the Rayleigh–Taylor instabilities proposed to explain the formation and appearance of the Crab filaments (Chevalier & Gull 1975; Bandiera *et al.* 1983). They have been dramatically revealed in recent high-resolution *Hubble Space Telescope (HST)* narrow-band imaging (Hester *et al.* 1994). The brightest filaments, as displayed by the isophotal levels in Fig. 1, are mostly located at this inner boundary of the ejecta shell. The E–W torus and the southern filament near Miller's position 1 both have radially extended, sheet-like morphologies that mark the farthest protrusions of the bright filaments into the inner synchrotron cavity. The outermost edge of the shell of filamentary [O III] emission is an ellipsoid roughly 7.′0×5.′0 (13.2 to 9.5 ly) across, also with major axis position angle ~130°. This is in excellent agreement with van den Bergh's (1970) measurements, and shows that our scan has reached at least as deep as some of the best sky-limited photographic imaging studies. From an examination of frame 1 of Fig. 2(a) and frame 11 of Fig. 2(b), it can be seen that the highest radial velocity gas, both blueshifted and redshifted, is located in the northwestern region of the remnant. This result, from a scanning technique with complete spatial coverage, confirms similar findings of Clark *et al.* (1983), who used a systematic spectroscopic technique that only sampled ~10% of the face of the nebula.

The view of the model presented in Fig. 1(c) is particularly striking. The filamentary shell is fainter in [O III] λ5007 near each end of the major axis; in particular, the SE region of the nebula has generally weaker [O III] filaments [frame 12 of Fig. 2(b)]. When the model is viewed along its SE–NW axis, the bright filaments displayed in Figs. 1(a) and 1(b) are projected upon one another and a clear line of sight is available through the entire nebula. These "holes" in the filamentary shell at each end of the major axis persist at lower isophote levels, filling in only when the intensity threshold is faint enough to display the remnant as a nearly solid shell. Figure 1(d) is indicative of the appearance of the remnant from other viewing angles; the bright filaments prevent a clear view through the center of the inner cavity. The "velocity discontinuity" seen at the NW end of the major axis in a spectrum taken by Wyckoff *et al.* (1976) is probably related to the hole seen in our data.

The line of sight defined by the best alignment of the holes in Fig. 1(c) is located at a position angle of ~125° E of N and inclined ~25° from the plane of the sky. The hole centers have symmetric velocity offsets (approximately −900 km s$^{-1}$ in the SE and +900 km s$^{-1}$ in the NW when measured near the outermost edges of the nebular shell), and the projection of the line of sight through them onto the plane of the sky is nearly coincident with the proper motion vector of the pulsar (WM). So the line of sight through the holes intersects the zero radial velocity plane near the center of expansion and the current location of the pulsar. The value of the inclination depends on the distance and the assumption of constant radial velocity incorporated into the model; placing the nebula closer would increase the inclination, while making a correction for outward acceleration in the radial velocities would decrease the inclination. We note the correlation of the line of sight through the holes with the major optical axis of the nebula, and the alignment of the pulsar with Scargle's (1969) wisps and the centroids of the X-ray, optical, and radio synchrotron emission to the NW. The line of sight through the holes corresponds with the ~24° inclination proposed for a toroidal structure in the X-ray emission model of Aschenbach & Brinkmann (1975), supported by *Einstein* data (Brinkmann *et al.* 1985), and also the ~26° inclination of a proposed, ring-like "halo" model for Scargle's wisps (Scowen *et al.* 1994). All of these authors propose that the spin axis of the pulsar, and a corresponding polar jet or Poynting-flux-driven wind, is aligned with position angle and inclination very similar to that found here for the line of sight through the holes in the filamentary shell.

As noted by Michel *et al.* (1991), the presence of two distinct symmetry axes in the remnant presents a theoretical puzzle. The N–S axis seen in the bright-filament morphology, abundance distributions, and radial velocity field and the NW–SE axis seen in the profile of the outer shell, proper motions, and synchrotron activity near the pulsar are well established by observational evidence. Michel *et al.* (1991) suggest that precession of the pulsar spin axis or modification of the remnant by swept-up interstellar magnetic fields might resolve the issues, and Fesen *et al.* (1992) have proposed pre-SN mass loss by a helium-rich progenitor induced by an unseen binary companion. It is important to conduct further observational and theoretical investigations to reconcile these structures.

Frame 4 of Fig. 2(b) contains the image, with central wavelength of 5015.3 Å, in which the "argoknots" were first noticed in 1989. Further Fabry–Perot imaging and two-dimensional spectroscopy has since been obtained at the MDM Observatories and the *Multiple Mirror Telescope*. A description of the positions, proper motions, radial velocities, and a preliminary spectral description of these knots has been published by M94. The deepest image with the highest resolution of the argoknots to date is presented in their Fig. 1. The northern sequence of knots is spatially coincident with a filament located at significantly higher redshifted velocity. The appearances of the knots within the data cube and their relationship with the redshifted filament are displayed in Fig. 2(b). With radial velocities between +300 and +720 km s$^{-1}$, the knots appear, brighten, and then fade in the velocity space between images at 5009.0 and 5019.8 Å (frames 1 through 6). The bright knot labeled N6 by M94 is the clearest example, appearing in the sequence of frames 1 through 3. The redshifted filament, which includes filament 334 of T70, ranges in radial velocity from +900 km s$^{-1}$ at its northern end to +1300 km s$^{-1}$ near its southern intersection with the E–W torus. It is most prominent in the images at 5022.4 and 5026.3 Å (frames 8 and 9). A comparison of the morphology of the filament with the locations of the knots shows that most are not spatially coincident with bright features in the filament. In fact, recent spectroscopy

© American Astronomical Society • Provided by the NASA Astrophysics Data System

1995AJ....109.2635L



(MacAlpine & Lawrence 1995) indicates that several of the knots are spatially coincident with lower-intensity "breaks" in the emission from the filament. This may indicate that the material in the knots is derived from the filament, perhaps through some instability, as has been suggested by M94. Alternatively, the lower intensities behind the knots may be evidence for dust within the knots. The dust would obscure the line radiation from the filament directly behind the knot, just as other filaments containing dust have been shown to screen the synchrotron continuum (Fesen & Blair 1990; Hester *et al.* 1994). A detailed analysis of all spectroscopic and imaging data available for the argoknots is underway (MacAlpine & Lawrence 1995).

## 5. CASSIOPEIA A

### *5.1 Background*

Nebulosity from the Cassiopeia A supernova remnant was first detected by Baade & Minkowski (1954) in their search for optical counterparts to strong radio sources. Detailed spectroscopic and proper motions studies, conducted primarily by collaborations led by van den Bergh or Fesen, have shown that the optical line-emitting gas can be divided into three components, categorized by their motions and spectroscopic properties.

One component is the system of fast-moving knots (FMKs), of which 120 have been defined by KB76 and Fesen *et al.* (1988, hereafter referred to as FBG). These knots are distinguished by their high spatial velocities, with proper motions in the range of 0″.2–0″.7 yr$^{-1}$ and radial velocities as large as 5500 km s$^{-1}$. They are spectrally identified by strong emission in oxygen, sulfur, and argon, with no detectable hydrogen or helium lines [with one exception noted by Fesen & Becker (1991, hereafter referred to as FB91)]. They are generally located at radial distances <135″ from the derived center of expansion of the remnant, and are contained within the incomplete shell-like structures seen in radio and X-ray observations. The most notable exception is the "jet" to the northeast (van den Bergh & Dodd 1970), which is composed of roughly ten identified FMKs located between position angles 60° and 80° E of N, and extending outward nearly 4′ from the center. Proper motion analyses of knots in the main shell indicate an expansion age of ~330 yr, with a slightly smaller value determined from the subset of FMKs located in the jet.

A second component is composed of the approximately 40 quasi-stationary flocculi (QSFs) defined by van den Bergh & Kamper (1985, hereafter referred to as BK 85). These are characterized by much smaller spatial velocities, with proper motions <0″.03 yr$^{-1}$ and radial velocities in the range from +50 to −450 km s$^{-1}$. The strongest lines in QSF spectra are from nitrogen and hydrogen, with the former often significantly stronger than the latter. Weaker emission from helium, oxygen, sulfur, iron, and calcium has also been detected. Most QSFs are located within 135″ of the expansion center of the FMK system, although several individual QSFs and some diffuse emission have been detected more than 3′ to the southwest. This system has an estimated expansion age of ~11,000 yr.

The third, recently detected component consists of 15 fast-moving flocculi (FMFs) defined by FBG, which combine the kinematic properties of FMKs with spectral signatures similar to QSFs. FMFs have some of the highest spatial velocities, with proper motions in the range of 0″.5–0″.7 yr$^{-1}$ and radial velocities between −2200 and +4700 km s$^{-1}$. Spectrally, FMFs show strong nitrogen lines, with weak or undetectable emission in hydrogen and helium. These features are all located exterior to the main shell defined by the FMKs and QSFs, with radial distances between 140″ and 190″ from the FMK expansion center. The expansion derived for these knots is ~310 yr, which is in close agreement with the age determined from the subset of FMKs contained within the jet.

The standard model put forth in the literature is that Cas A was created in the supernova explosion of a massive star, possibly of the WNL subclass of Wolf–Rayet stars (see the discussion and references in FB91). In this picture, the QSFs represent nitrogen- and helium-enriched material shed by the progenitor star ~$10^4$ yr prior to the explosion. The FMFs are high-velocity fragments from the progenitor's photosphere, which was nitrogen rich but still must have contained some hydrogen. The FMKs are oxygen- and sulfur-enriched ejecta originating from processed mantle material, with the lack of hydrogen or nitrogen lines indicating that they are relatively undiluted by swept up circumstellar or interstellar gas. All of these features are thought to be shock heated, although some diffuse nebulosity associated with the QSFs may be material photoionized by the UV and X-ray emission of the supernova event. The proper motions and radial velocities of FMKs in the jet suggest a fairly collimated ejection of material at much higher velocities in one particular direction, implying that the explosion itself may have been significantly asymmetric. All of the optically emitting features form only a small fraction (<1 $\mathscr{M}_\odot$) of the total ejected mass, most of which (15–20 $\mathscr{M}_\odot$) is contained in a high-temperature, low-density shell seen in X-ray and radio emission.

In the discussions below we refer to previously defined FMK, QSF, and FMF features using the numbering schemes introduced in KB76 and Fesen *et al.* (1987, hereafter referred to as FBB), with modifications from van den Bergh & Kamper (1983, hereafter referred to as BK83; BK85), and FBG.

### *5.2 Discussion of the Fast-Moving Knots*

The processed $I(\alpha,\delta,\lambda)$ data cube in [S II] λλ6716, 6731 emission from the FMKs was transformed into $(X,Y,Z)$ linear space using a distance of 2,800 pc (van den Bergh 1971b) and an expansion age of 334 yr (BK83). The distance was derived from an expansion parallax method that equated the maximum radial velocity with the proper motions necessary to provide the main body of the nebula with its current ~135″ radius. Our isophotal models therefore resulted in roughly spherical shapes. The origin of the $X-Y$ plane was selected to match the origin of the of the coordinate system used in the proper motion studies of KB76, located at $\alpha_{1950}=23^h21^m12^s.0$, $\delta_{1950}=58°32'24''.0$. From BK83 the de-

© American Astronomical Society • Provided by the NASA Astrophysics Data System

1995AJ....109.2635L



rived center of expansion is approximately 6″ south of this location, so the origin of our models is close to the true center of expansion of the nebula. At a distance of 2,800 pc the trimmed 330″ square field of view translates into an $X-Y$ plane that is 14.6 ly across. This field of view encompasses the spherical body of the remnant, but does not include features from the outer portions of the jet (FMKs 113–121 of BK83 and FBG). The individual images within the scan were binned in 5×5 pixel blocks, degrading the $X$ and $Y$ resolution closer to that of the $Z$ axis and improving the appearance of the displayed isosurfaces. The resulting resolution in the plane of the sky is 0.15 ly.

In order to complete the observations in a reasonable number of nights, a large bandpass (14.4 Å FWHM) was selected and the scan increment was set to be nearly the same width (12.0 Å). The scan covers a wavelength range of 6609–6861 Å, which samples gas with radial velocities from $-5400$ km s$^{-1}$ in [S II] λ6731 to +6500 in [S II] λ6716. With the bandpass and scan increment used, we were unable to resolve the individual components of the [S II] doublet and the zero radial velocity plane was defined by an average rest wavelength set at 6723.6 Å. Published values for the measured strengths of these lines indicate that the $I(6716)/I(6731)$ ratio varies from 0.3 to 1.6 for different FMKs (Kirshner & Chevalier 1977; Peimbert & van den Bergh 1971). These observations span the theoretically predicted range of values from the low- to the high-density limits (Osterbrock 1989), so the intensity-weighted mean position of the unresolved line should fall near the assumed average. The resolution in velocity space, combining the effects of the scan increment and the range of the $I(6716)/I(6731)$ ratio, is estimated to be 1250 km s$^{-1}$. This is equivalent to a resolution of 1.4 ly along the $Z$ axis of the spatial model. The uncertainty in velocity measurements, as determined by Monte Carlo simulations of fitting a single Gaussian profile to the unresolved doublet with varying line ratios, is 760 km s$^{-1}$. Table 2 contains a summary of parameters used for this model.

A second consequence of setting the scan increment nearly equal to the bandpass is that the isophotal surfaces for this scan are technically not complete. An emission feature with an intensity level near the isophotal threshold and an intrinsic velocity width much narrower than our bandpass could be missing from the contour display, if its central velocity were located midway between the central velocities sampled by two adjacent scans. Such features would have their flux distributed roughly equally between the two scans, and no single point in the irregular $I(\alpha,\delta,\lambda)$ array would be above the isophotal threshold. The other observations in this paper have scan increments significantly smaller than their bandpasses, and their displays are complete to the given isophotal threshold.

Three views of the isophotal model of the Cas A FMKs in [S II] emission are presented in Fig. 3 (Plate 85). The isophotal level was set at $3.5\times10^{-16}$ erg s$^{-1}$ cm$^{-2}$, a value low enough to display the locations of the majority of FMKs, but high enough to suppress sky noise and provide a clear definition of structures viewed in projection on top of one another. Figure 3(a) presents the remnant seen along the line of sight from Earth, showing the front side of the FMK system. North is up and east is to the left. Figure 3(b) displays the remnant as viewed 180° from the vantage point of Fig. 3(a), showing the back side of the FMK system. North is up and east is to the right. Figure 3(c) illustrates the remnant from a vantage point 20° directly north from that of Fig. 3(b), and shows the FMK system from behind and slightly above. The color coding represents radial velocity with respect to the Earth; in Figs. 3(a)–3(c) darkest blue is $-5100$ km s$^{-1}$, deepest red is +6100 km s$^{-1}$, and green is the zero radial velocity plane. Due to unfavorable weather conditions, the velocity scan of the FMK system was not completed. The final image in the sequence, centered at a wavelength of 6861.0 Å, still shows significant structures, indicating that there is most likely more line-emitting gas at higher redshifts that was not sampled by the scan. As a result, the color coding in some regions of Figs. 3(b) and 3(c) can be misleading. Since the isophotal level is low enough to include emission from knots present in the most highly redshifted velocity slice, the hollow wire-frame structures generated by the AVS isosurface routine are truncated at the back of the data cube and do not form closed surfaces. Any perspective that views the back of the data cube will sight through the open end and display the color coded *interior* walls of the hollow isosurfaces. The yellow–orange regions seen bounded by sharp red outlines in upper portions of Fig. 3(b) are examples of this; the yellow–orange is a view of the inside surface toward the front of a highly redshifted FMK.

The interpolated $I(\alpha,\delta,\lambda)$ data cube is presented as a mosaic of frames in Fig. 4 (Plates 86 and 87), with bandpass centers listed in Table 3. These frames display the entire scanned range of radial velocities relative to a rest wavelength of 6726.3 Å, in 535 km s$^{-1}$ steps. They range from $-5030$ (frame 1) to +860 km s$^{-1}$ (frame 12) in Fig. 4(a), and from +1390 (frame 1) to +5680 km s$^{-1}$ (frame 9) in Fig. 4(b). With only 21 interpolated images, frames 10 and 11 of Fig. 4(b) have been left blank. Frame 12 of Fig. 4(b) presents a stacked image formed by adding all images in the irregular $I(\alpha,\delta,\lambda)$ data cube. The most prominent features in frames 1 and 2 of Fig. 4(a) are the result of [N II] λ6583 from the strongest QSFs (see the discussion below) detected by the broad wings of the 14.4 Å FWHM etalon profile used in this scan.

An inspection of Fig. 3(a) shows that the FMK system can easily be grouped into four distinct regions of [S II] emission. The largest and brightest is the northern arc of emission located in the upper central region of the figure, and colored with the full range of radial velocity. This structure encompasses the majority of individual knots defined by KB76, including FMKs 3–18 and most of 28–90. The next region is formed by the structures located at the base of the jet, to the northeast and east of center in the figure, and primarily colored with blues and greens. Included are FMKs 1, 19, 20, and most of 92–112. Third is the recently formed (BK85) arc of nebulosity which delineates the southwest boundary of the FMK system and is shaded with blues, greens, and yellows. FMKs 36, 38, and 40 are defined within this feature. Finally, there are the irregular patches of emission to the southeast, primarily displayed in shades of blue,

© American Astronomical Society • Provided by the NASA Astrophysics Data System

1995AJ....109.2635L



which contain FMKs 96 and 99. Small features at various radial velocities that appear near the edges of the frame in the northeast and southwest are probably not real sources of line emission, but are more likely the result of small errors in the removal of stars or of peaks in the night sky noise. A visual comparison of the locations and morphologies of the FMKs defined in BK83 with features in our data indicates that we have detected the vast majority of previously defined FMK features and have reached deeper to detect significantly lower surface brightness emission in many locations. We confirm the distribution of much of the diffuse [S II] emission which was marginally detected by KB76, indicated in their Fig. 2.

The most striking feature of the model displayed in Fig. 3 is that the northern arc is revealed to be two complete rings of emission, inclined and projected on top of one another, yet distinctly separate in velocity space. The distribution of the FMKs into ring-like structures was first noted in the spectroscopic studies of Reed *et al.* (1989, 1991). Measured from the outer edges of its emission, the blueshifted smaller ring spans roughly 90″×50″ on the sky, corresponding to 4.0×2.2 ly, and ranges from approximately −3500 to 0 km s$^{-1}$ in radial velocity. It can be traced in frames 3–11 of Fig. 4(a). The redshifted larger ring spans 140″×80″ on the sky, corresponding to 6.2×3.5 ly, and its circumference forms the entire outer periphery of the northern arc of [S II] emission. This ring spans a greater range in radial velocity, extending from 0 km s$^{-1}$ to beyond +6000 km s$^{-1}$, and includes the most highly redshifted material detected in Cas A. The nearly continuous nature of the larger ring can be clearly seen in the upper left section of Fig. 3(c), and traced from frame 11 of Fig. 4(a) through to frame 11 of Fig. 4(b). Within the limited velocity resolution of our data cube, the two rings meet and blend together near the zero-velocity plane [frames 10–12 of Fig. 4(a)] at the most northerly extent of the [S II] emission. These rings may have originated from some form of instability in the expanding spherical shell of the remnant, or from the interaction of the ejecta with denser inhomogeneities in the circumstellar medium.

We note that, from the perspective of Fig. 3(c), there also appears to be a much larger elliptical ring formed by the southwestern arc and emission at the base of the jet. These features are stronger regions of [S II] emission from portions of the limb brightened ring of the remnant, centered near the zero radial velocity plane. Aside from their locations on nearly opposite sides of the spherical ejecta shell, the southwestern arc and the base of the jet do not form a distinct, continuous substructure on the surface of the shell as the previously described rings in the northern arc do. While the emission properties of these features are important to an understanding of the remnant, we suspect that the larger elliptical ring seen in Fig. 3(c) is mainly due to projection effects and the poor resolution in radial velocity along the $Z$ axis, and not caused by the same physical processes responsible for the substructure within the northern arc.

Comparing our data cube with photographic plates presented in BK85, we see that many of the FMKs detected strongly in [O III] within the northern arc are located in projection on the larger ring. This is particularly true of those knots in the southern half of the northern arc identified as radiating in [O III] but not in [S II], many of which have only recently formed (see Fig. 3 of KB76 and Fig. 5 of BK85). These knots are coincident on the sky with the most highly redshifted sections of the larger [S II] ring. As there exist some filaments that emit [O I], [O II], and [O III], but not [S II], clearly some abundance variations must be present among certain FMKs. However, linking the [O III]-strong knots with the larger [S II] ring could alternatively be taken as evidence that the differences in sulfur and oxygen emission may be due in part to excitation conditions as well as abundance variations. It is generally accepted that the FMKs are shock heated through their interaction with the ambient medium, and theoretical models have shown that the emissions from shocked gas are highly sensitive to the shock velocity and gas density (see, for example, Cox & Raymond 1985; Dopita *et al.* 1984). The presence of a set of rapidly evolving, [O III]-strong knots, which may be experiencing greater decelerations than typical FMKs, within a localized region of the remnant shell could indicate variations in the ambient medium or in the gas density of ejecta in this direction in space.

The emission surrounding the base of the jet can be classified into five main structures. The first is the most northern, E–W structure that is shaded in blue and green in Fig. 3(a). This corresponds to Baade and Minkowski's Filament 1 (1954) and includes FMKs 19, 20, 92, 93, 102, 104, and 105. It spans a range of velocities from −1000 to +2000 km s$^{-1}$, with its most intense emission peak centered at approximately 0 km s$^{-1}$ [frames 5–12 of Fig. 4(a) and 1–3 of Fig. 4(b)]. The second and third emission structures are the pair of irregularly shaped features at the southern end of the base of the jet, nearly due east of the center of expansion, and colored blue in Fig. 3(a). The more northerly of the pair has radial velocities in the range of −2500 to −1000 km s$^{-1}$, while the southern feature spans a larger range of velocity, extending from −2500 km s$^{-1}$ in its northeastern end to +500 km s$^{-1}$ in its southwestern end [frames 5–12 of Fig. 4(a)]. There are also two compact knots to the southeast from this structure which are centered between +1000 and +1500 km s$^{-1}$, shaded green in Fig. 3(a). The next structure associated with the base of the jet is the N–S extended feature seen in projection behind the previous three in Fig. 3(a). It is more clearly seen in Fig. 3(b) as the vertical, yellow–orange feature running south from Baade and Minkowski's Filament 1, and it contains the "slow-moving streaks" (e.g., FMK 100) mentioned by KB76. This fourth structure ranges from −1000 to +2500 km s$^{-1}$ in radial velocity (although a small, isolated knot on the interior edge is centered near +3500 km s$^{-1}$), and is seen in frames 6–12 of Fig. 4(a) and 1–5 of Fig. 4(b). The fifth structure is the small patch of nebulosity at the very eastern edge of Fig. 3(a), shaded in blue. The upper portion of this feature is a faint, linear filament within the jet itself, approximately 30″ radially inward from FMK 115. It extends ~20″ to the edge of the field of view and may be connected to the linear filament seen in the southwest corner of Fig. 5(b) of FBG or with the FMK emission serendipitously detected in the "diffuse nebula" spectrum of FBB (see the discussion of the QSF system below). The lower

© American Astronomical Society • Provided by the NASA Astrophysics Data System

1995AJ....109.2635L



portion of the fifth structure appears to be the combination of faint [S II] emission from the northern extension of the diffuse nebula of FBB and continuous emission from a fainter star that was missed in the masking procedure. Each portion of this structure contains a few small, condensed FMK features with radial velocities between −4000 and −3000 km s$^{-1}$.

The remaining emission regions are the southwestern arc of filaments and the irregular patches to the southeast. The southwestern arc stretches across ~150″, corresponding to 6.6 ly in our model, spanning position angles of 175° to 260° E of N as measured from the center of expansion. Our data show this feature to be larger than in previous studies, and this is probably due to the higher sensitivity allowed by the narrow Fabry–Perot bandpass, as well as the continuing growth and evolution of the arc (BK85). Individual portions of this feature are distributed across roughly 6500 km s$^{-1}$ in radial velocity space, ranging from −2000 km s$^{-1}$ in the small northern "spur" seen in blue in Fig. 3(a) [frames 6–8 of Fig. 4(a)] to +4500 km s$^{-1}$ in the two small knots at the northwestern end of the arc seen in red in Fig. 3(b) [frames 5–8 of Fig. 4(b)]. The majority of the body of the southwestern arc is contained in a velocity range of −1000 to +3000 km s$^{-1}$ [frame 7 of Fig. 4(a) to frame 7 of Fig. 4(b)]. The irregular patches of diffuse nebulosity to the southeast are mostly located well within the ~135″ radius of the remnant's outer edge and contain the most highly blueshifted ejecta, with radial velocities ranging from −4500 to +500 km s$^{-1}$ [frames 2–12 of Fig. 4(a)].

There is a substantial velocity asymmetry from the front to the back of the remnant; the radial velocities of the most blueshifted [S II] knots are −4500 km s$^{-1}$, while those of the most redshifted knots are $\gtrsim$+6000 km s$^{-1}$. Accounting for the average proper motions these filaments would need to reach their present locations in 334 yr at a distance of 2.8 kpc, these correspond to space velocities of 5100 km s$^{-1}$ and $\gtrsim$6900 km s$^{-1}$, respectively. The outer boundary of the FMK system is not as distinctly defined in the SE region of the remnant, and the ejecta appear more diffuse and less concentrated into discrete knots. The largest radial extent of the [S II] emission in this area is, however, a fairly compact knot located ~130″ from the center of expansion, similar to the greatest extents of the FMKs in northern areas of the main shell. As with the southwestern arc, our data cubes reveal more extensive emission in this region than can be seen in the plates of KB76, BK83, and BK85. In Fig. 6 of BK85, the authors point out the recent appearance of new FMKs in this region, so the greater amount of emission detected here is also likely to be a combination of greater sensitivity and continued evolution of the remnant.

### *5.3 Discussion of the Quasi-stationary Flocculi*

The processed $I(\alpha,\delta,\lambda)$ data cube for Cas A in $H_\alpha$+[N II] λλ6548, 6583 emission from the QSFs was transformed into $(X,Y,Z)$ linear space using the same parameters and binning as described above for the FMKs. The system was scanned through a wavelength range of 6548–6600 Å with a bandpass of 5.3 Å FWHM. This wavelength range samples $H_\alpha$ emission from gas with radial velocities between −800 and +1800 km s$^{-1}$, [N II] λ6583 emission between −1700 and +900 km s$^{-1}$, and [N II] λ6548 emission between −100 and +2500 km s$^{-1}$.

Because three emission lines overlap in velocity space, the wavelength axis of the data cube does not translate easily into a spatial axis, as it does with the unresolved [S II] λλ6716, 6731 scan. We used the rest wavelength of $H_\alpha$ to define the zero velocity plane for all emissions, so the $Z$ axis corresponds more to a scaled wavelength axis, rather than a velocity or spatial axis. For example, gas radiating [N II] λ6583 at zero radial velocity was translated into the model at the equivalent position of gas radiating $H_\alpha$ at +940 km s$^{-1}$. The effective result is three nested models of the QSF gas, with the two distributions arising from the [N II] lines bracketing and overlapping the $H_\alpha$ distribution. The relative spatial distribution of different flocculi emitting in the same emission line is correctly scaled within the model, with a linear spatial offset between different emission lines arising from the same flocculi. The velocity resolution is 270 km s$^{-1}$, which translates to a $Z$ axis spatial resolution of 0.30 ly.

The isophotal model of the Cas A QSFs in $H_\alpha$+[N II] λλ 6548, 6583 emission is presented in Fig. 3(d), viewed along the line of sight from Earth. North is up and east is to the left. The isophotal level was set at $1.1\times10^{-16}$ erg s$^{-1}$ cm$^{-2}$, a value low enough to display the faintest QSFs, but high enough to suppress the sky noise. Some trace of the noise is present, however, and is visible as the small "specks" concentrated mostly in the corners. The colors correspond to wavelength. Darkest blue represents λ=6548 Å (a velocity of −700 km s$^{-1}$ in $H_\alpha$ emission) and deepest red represents λ=6600 Å (+1700 km s$^{-1}$ in $H_\alpha$), so gas emission in [N II] λ6548 will be shaded blue, emission in $H_\alpha$ will be shaded light blue through yellow, and emission in [N II] λ6583 will be shaded yellow through red. As for the [S II] scan of the FMK system, several isophotes extend to the front and rear surfaces of the data cube, so they are not closed. Just as the wings of the slit profile can partially blend closely spaced emission lines in conventional slit spectroscopy, the wings of the Airy transmission profile of the etalon blend the $H_\alpha$+[N II] λλ6548, 6583 emissions of the brighter QSFs in this scan. To reveal the lowest surface brightness emission in the QSF system, the isophotal level was set at a relatively low value, which was faint enough to trace out the brighter features in the wings of the instrumental transmission profile. For the brightest QSFs, these wings overlap between the three emission lines present in the scan and often extend to the front and back of the data cube. So these brighter features form hollow, bulging, tube-like surfaces that extend across a large span of the color-coded wavelength axis and may be open at either or both ends. Examples of these bright QSFs can be seen as small rings of color with red or black centers.

A representative portion of the interpolated $I(\alpha,\delta,\lambda)$ data cube is displayed as a mosaic of frames in Fig. 5 (Plate 88), with the bandpass centers listed in Table 3. These frames sample the expected velocity range of [N II] λ6583 emission from the QSF system, ranging from roughly −1040 (frame 1) to +260 km s$^{-1}$ (frame 11), and also include $H_\alpha$ emission from velocities $\gtrsim$−100 km s$^{-1}$. The velocity step between

© American Astronomical Society • Provided by the NASA Astrophysics Data System

1995AJ....109.2635L



frames is 130 km $s^{-1}$. Frame 12 of Fig. 5 presents a stacked image of the entire $H_\alpha$+[N II] λλ 6548, 6583 scan formed by adding all images in the irregular $I(\alpha,\delta,\lambda)$ data cube.

A comparison of our data cube with the results of BK85, FBB, FBG, and FB91 shows that we have detected the majority of previously defined QSF and FMF features within our field of view. The exceptions are QSFs 14, 15, and 32 (see Table 2 of BK85) and FMFs 2, 3, 4, 10, 13, 14, and 15 (see Table 1 of FBB). In BK85 it is noted that QSFs 14 and 15 are likely to be FMKs emitting in [O I] but not in [S II], which were mistakenly identified as QSFs. It is not surprising that these two features are not present in our data, as a radial velocity well over +8000 km $s^{-1}$ would be required to shift [O I] λ6364 into the spectral range of our scan. Accounting for the Airy curvature of our scan and using the radial velocities given in FBG, it can be seen that FMFs 2 and 3 are too blueshifted and FMFs 4, 13, and 15 are too redshifted to appear in the QSF scan. FMFs 4, 13, and 15 are detected in the appropriate frames of the FMK [S II] scan. No radial velocity information is available for QSF 32 or FMF 14, so it is possible that their emissions are also too blueshifted to appear in our scans. We note from BK85 that the proper motion for QSF 32 is larger than for typical QSFs, although not as large as for typical FMKs, and it might also be an FMK detected by BK85 through redshifted [O I] emission. Another explanation for the nondetection of these features is that they may have decreased in brightness since observations taken in 1983, 1987, and 1988 (BK85, FBB, and FBG, respectively). This is not very likely, however, given evidence that typical QSFs have lifetimes on the order of 25 yr (BK85), and that FMF 10 is young (FBG).

In addition to the previously defined QSFs, our Fabry–Perot scan reveals other features that radiate in $H_\alpha$+[N II] λλ 6548, 6583. These fall into two categories: compact, discrete knots similar to known QSFs and larger, low surface brightness regions similar to the diffuse nebula located to the east of the remnant (see Fig. 7 of FBB). Most of the potential new QSFs are found within the radio shell of the remnant among previously defined QSFs in the northern and southwestern arcs of FMKs. That these have not been previously cataloged as QSFs is most likely due to a combination of effects. The studies of van den Bergh and Kamper used wide filters and were primarily focused on proper motion measurements, so their list of QSFs would naturally include the brightest features that were present on images from multiple epochs and easily distinguished from the clutter of overlapping FMK emissions. The much narrower bandpass of the GFPI suppressed continuum from the night sky relative to the line emission from the QSFs and also excluded emissions from nearly all of the FMKs, permitting an uncluttered image of fainter QSFs.

Four regions of diffuse emission can be seen in our scan. The first is formed by the western and northern portions of the diffuse nebula of FBB, displayed in light blue along the eastern edge of Fig. 3(d) and present in frames 1–3 of Fig. 5. In agreement with FBB, we find this region to have much stronger emission in $H_\alpha$ than in [N II] (compare frames 2 and 9 of Fig. 5, which represent emissions from $H_\alpha$ and [N II] λ6583 at roughly the same radial velocity). The second region of diffuse emission is an elongated feature beginning near the eastern end of QSF 1, extending ~120″ southward to just east of QSF 34, prominent in frames 8 and 9 of Fig. 5. Once again, comparing frames 9 and 2 of Fig. 5, it can be seen that this nebulosity has significantly stronger emission in [N II] λ6583 than in $H_\alpha$, similar to the spectra of many QSFs. Possibly related to this second region is a series of small, fainter patches of diffuse emission that arc across the southern edge of the field in Fig. 3(d). This third region begins 25″ NE of QSF 36 and stretches in a faint arc which connects QSFs 36, 37, 38, and three small, undefined QSFs located approximately 20″ S of QSF 20. The western portion of this arc was seen by FBB, who noted that it continues southward out of our field of view in a line connecting QSFs 20 and 40. As with the second region described above, features in this region have stronger [N II] λ6583 than $H_\alpha$ emissions. The fourth and faintest diffuse region consists of a faint arc that runs NE between the stars labeled "g" and "h" by van den Bergh (1971a) and then curves eastward and ends ~15″ ENE of QSF 13. Spectra extracted from this section of the data cube show a range of $H_\alpha$/[N II] strengths; at some points $H_\alpha$ is markedly stronger, in others [N II] λ6583 is stronger, and in others the two lines are nearly equal. The strengths of the [N II] lines in several of the diffuse nebular regions indicate gas with enhanced nitrogen abundance, similar to that found in the QSFs and most FMFs. If so, this is strong evidence that some of this diffuse gas originated in a period of mass loss by the progenitor star.

Another striking feature revealed by our model is in the projected distribution of $H_\alpha$+[N II] λλ 6548, 6583 emission features on the sky, seen in Fig. 3(d) and frame 12 of Fig. 5. Unlike the FMKs, which present the profile of a limb-brightened spherical shell, the majority of the QSFs and associated diffuse emissions are located within a 4′.7×2′.3 elliptical region with position angle 25° E of N. At the distance of Cas A, this corresponds to a 12.4×6.1 ly ellipse. The northeastern end is populated by QSFs which are spatially coincident with the northern arc of FMKs, but the southwestern end extends an arcmin beyond the rim of the FMKs. The QSFs are not distributed evenly throughout the region but seem to be in several lobe-like structures that place them near the edges of the elliptical boundary.

If the QSF distribution were contained in a circular plane, it would need to be inclined ~60° to have the observed ellipticity. It seems unlikely, however, that the observed distribution is actually a circle or ellipse centered on the origin of the explosion. Nearly all QSFs have radial velocities in the range of −100 to −200 km $s^{-1}$ (BK85), and there is no correlation between radial velocity and position angle as would be expected. For example, at the end of the major axis in the northeast, where the radial velocities would be closest to the systemic radial velocity of the entire structure, measurements indicate a spread from +40 km $s^{-1}$ (QSF 1Q1 of Kirshner & Chevalier 1977) to −283 km $s^{-1}$ (QSF 18). McKee & Cowie (1975) have proposed that the observed radial velocities of QSFs are indicative of the velocities of the shock waves heating them and not the bulk motion of the gas clouds prior to the supernova. They attribute the negative radial velocity distribution of the QSFs to initial anisotropies

© American Astronomical Society • Provided by the NASA Astrophysics Data System

1995AJ....109.2635L



in the circumstellar material. Similarly, the elliptical distribution of QSF material on the sky is more likely due to asymmetries in (i) the mass loss of the progenitor star, (ii) the interaction of this material with the interstellar medium following its ejection, or (iii) the excitation of this material through interactions with the supernova ejecta.

## 6. THE REMNANT OF NOVA GK PERSEI

### *6.1 Background*

Although categorized as a classical nova, GK Per (Nova Persei 1901) differs from most others of its class in several ways. It has the longest known orbital period, an evolved K0 IV secondary (Crampton *et al.* 1986), and has continued to manifest dwarf-novae-like outbursts during its quiescence (Sabbadin & Bianchini 1983). Shortly after the main outburst, nebulosities with apparent superluminal motion were observed, and were interpreted by Couderc (1939) as reflections from dust in material along the line of sight to the nova. Although modern searches around recent novae have been undertaken (van den Bergh 1977; Schaefer 1988), only one other nova (Nova Sgr 1936; Swope 1940) has exhibited light echoes. This led Schaefer (1988) to propose that the grain density in the light echo region may be up to $10^4$ times that of the general interstellar medium. The ejected nebula was first discovered by Barnard in 1916 (see Curtis 1919) and has been imaged by various investigators at irregular intervals up to the present (Anupama & Prabhu 1993, hereafter referred to as AP93; Seaquist *et al.* 1989, hereafter referred to as S89; bibliographic references in Duerbeck 1987b). The nova shell is remarkable for its brightness, longevity and asymmetry, and there is strong evidence for an interaction with the ambient medium (Oort 1951; Duerbeck 1987a; S89; AP93). Reynolds & Chevalier (1984) detected a nonthermal, polarized ridge of radio emission coincident with the southwestern portion of the shell, which is highly unusual for novae remnants (Bode *et al.* 1987a) and similar to the emission seen in young SNRs like Cas A.

Detailed studies of GK Per and its environment were done by Bode *et al.* (1987b) and S89. These authors observed extended structures in both far-infrared and H I emission, elongated in a SE–NW direction and centered on the nova, which they interpreted as a torus of circumstellar material resulting from the ejection of a planetary nebula roughly $10^5$ yr ago. S89 drew attention to alignments between emission line features of the nova shell and the larger-scale structures seen in the infrared and radio, and proposed that the current appearance of the shell results from its interaction with the planetary nebula. They suggested the GK Per remnant is similar to a shock-heated SNR in the pre-Sedov phase (Chevalier 1977). AP93 and S89 described a NE–SW "polar" axis perpendicular to the circumstellar torus and intersecting the prominent southwestern limb, the ridge of radio emission and the region of the light echoes, and also a SE–NW "equatorial" plane coincident with the extended torus (see Fig. 13 of S89). Seitter & Duerbeck (1987), Bode *et al.* (1988), and AP93 suggested that differences between the distributions of optical and ultraviolet oxygen and nitrogen lines in the polar and equatorial directions are due to spatial variations in the abundances of these elements, while S89 proposed differing conditions of density and shock velocity within the clumped ejecta.

### *6.2 Discussion*

The processed $I(\alpha,\delta,\lambda)$ data cube for the GK Per nova remnant in $H_\alpha$+[N II] λλ 6548, 6583 emission was transformed into $(X,Y,Z)$ linear space using a distance of 470 pc (McLaughlin 1960) and an age of 90.7 yr. The distance was derived from an expansion parallax method, so our isophotal model resulted in a roughly spherical shape. The origin of the $X-Y$ plane was selected to match the centroid of the stellar image of GK Per itself, located at $\alpha_{1950}=3^h27^m47^s.5$, $\delta_{1950}=43°44'03''.8$. At the assumed distance, the trimmed 115″ square field of view translates into an $X-Y$ plane that is 0.86 ly across. Images within the scan were binned in 5×5 pixel blocks; the resulting resolution in the plane of the sky is 0.017 ly.

The scan covers a wavelength range of 6536–6612 Å with a bandpass of 5.3 Å FWHM. This range samples $H_\alpha$ emission from gas with radial velocities between −1200 and +2200 km s$^{-1}$, [N II] λ6583 emission between −2200 and +1300 km s$^{-1}$, and [N II] λ6548 emission between −600 and +2900 km s$^{-1}$. It was selected to span the measured 1200 km s$^{-1}$ range (McLaughlin 1960) of radial velocities in both $H_\alpha$ and [N II] emission. As with the similar scan of Cas A, the three overlapping emission lines within the spectral range prevented the wavelength axis from translating into a spatial axis in a straightforward manner. We again used the rest wavelength of $H_\alpha$ to define zero velocity for all emissions, so the $Z$ axis corresponds to a scaled wavelength axis. The velocity resolution is 270 km s$^{-1}$, equivalent to a $Z$ axis spatial resolution of 0.30 ly. The model parameters are summarized in Table 2.

Three views of the isophotal model of GK Per in $H_\alpha$+[N II] λλ6548, 6583 emission are presented in Fig. 6 (Plate 89). The isophotal contour was set at $6.0\times10^{-16}$ erg s$^{-1}$ cm$^{-2}$, a value that shows the majority of the line emitting gas without severely cluttering lines of sight through the model. Figure 6(a) displays the model viewed along the line of sight to the Earth, showing the front side of GK Per. North is up and east is to the left. Figure 6(b) presents the model viewed 180° from the vantage point of Fig. 6(a), showing the back side of GK Per. North is up and east is to the right. Figure 6(c) illustrates the model viewed from a vantage point 90° east from that of Fig. 6(a), and shows GK Per from the plane of the sky on the eastern side. North is up and Earth is to the left. The color coding represents wavelength. In these images darkest blue is λ=6536 Å (a velocity of −1200 km s$^{-1}$ in $H_\alpha$ emission) and deepest red is λ=6612 Å (+2200 km s$^{-1}$ in $H_\alpha$). As seen in Fig. 6(c), the remnant is dominated by emission from [N II] λλ 6548, 6583, with $H_\alpha$ only weakly present. The partial spheroid shaded green through red represents emission in [N II] λ6583, while the truncated, lower intensity duplicate shaded blue is [N II] λ6548. If a comparable shell of $H_\alpha$ emission were present, it would be a centered spheroid shaded between light blue and yellow. The relative weakness of $H_\alpha$

© American Astronomical Society • Provided by the NASA Astrophysics Data System

1995AJ....109.2635L



confirms the findings of others, who have reported [N II] λ6583 to be at least 20 times as strong as $H_\alpha$ (S89).

A representative portion of the interpolated $I(\alpha,\delta,\lambda)$ data cube is presented as a mosaic of frames in Fig. 7 (Plate 90), with the bandpass centers listed in Table 3. These frames sample most of the [N II] λ6583 emission, ranging from roughly $-840$ km s$^{-1}$ (frame 1) to $+980$ km s$^{-1}$ (frame 14), and include the highest velocity ($\gtrsim+770$ km s$^{-1}$) emission from [N II] λ6548 in frames 1–4 and weak emission from $H_\alpha$ with velocities $\gtrsim+100$ km s$^{-1}$ in frames 1–9. The velocity step between frames is 140 km s$^{-1}$. Frame 15 of Fig. 7 presents a stacked image of the entire $H_\alpha$+[N II] λλ6548, 6583 scan formed by adding all images in the irregular $I(\alpha,\delta,\lambda)$ data cube.

Several notable features can be seen in Figs. 6 and 7. While our model is approximately spherical with a diameter ~0.7 ly, there are striking deviations in the symmetry. Previous investigators have described the peculiar morphology of the remnant shell, with the dominant emission in [N II] arising from the southwestern polar limb (AP93, S89, and references therein), coincident with the nonthermal radio emission. Our data provide a much clearer impression of which areas of the shell lack emission. Figure 6(c) illustrates that the northern, blueshifted section of the remnant is particularly weak in [N II] emission, in a region defined by gas ejected northward from GK Per with radial velocities $\lesssim-200$ km s$^{-1}$. This lack of [N II] emission is also apparent in the northern portions of frames 1–4 of Fig. 7, where the faint emission that is present can be identified as redshifted $H_\alpha$ from gas detected in [N II] λ6583 in frames 8–11. In Figs. 6(a) and 6(b), the eastern quadrant of the remnant is also particularly weak, in a roughly conical volume defined by position angles between 60° and 130° E of N as measured from GK Per itself, and radial velocities between $-600$ and $+400$ km s$^{-1}$. This is evident in frames 5–9 in Fig. 7, where knots appearing to lie within the conical region east of GK Per actually lie outside it in velocity space. They have radial velocities $\gtrsim+800$ or $\lesssim-600$ km s$^{-1}$, and are present in these frames through $H_\alpha$ or strong [N II] λ6583 emission sampled by the wings of the etalon bandpass. The two regions do not appear to be separate, but form a continuous area of low [N II] emission spanning the northern, blueshifted "front" and eastern, low radial velocity "central" zones of the shell. The northeasterly location of the combined zones may be related to the NE–SW "polar" axis discussed by S89 and AP93, and could indicate that the NE pole is inclined toward the Earth.

The spatial locations of the low-emission regions disagree with three-dimensional models based on conventional longslit spectroscopy. Duerbeck & Seitter (1987) briefly described the shell in $H_\alpha$ emission as missing the "south polar cap" and a region "extending from the near center to the west." Bode *et al.* (1988) revised this by stating that it is the south polar cap and a region lying "towards the east and on the near side" that are deficient in line emission. The shell seen in our models of [N II] emission agrees with their conclusion that there is an eastern region with dramatically lower line emission. However, comparison of our data cube with images in S89 confirms that it is the *northern*, blueshifted region of the shell that is weak in [N II] emission, and that the southern regions contain some of the strongest [N II]-emitting knots distributed across a wide range of radial velocities. Duerbeck and Seitter based their model on $H_\alpha$ emission, which is too faint to extract reliably from the [N II] in our present models, so the structural differences may be real.

The box-shaped morphology of the remnant described by S89, is particularly apparent in frames 6–8 of Fig. 7, centered near the zero radial velocity plane of [N II] λ6583. The southwestern and northeastern limbs of the nebular shell are noticeably flattened, and the northwestern region appears similarly distorted. Individual knots throughout the remnant, and particularly those in the flattened portions of the outer shell tend to be elongated and pointed radially inward. This may be further evidence for the proposal by S89 that the remnant shell has been fragmented by Rayleigh–Taylor instabilities, originating in the interaction between the ejecta and the swept-up circumstellar medium (see Chevalier 1977, and references therein). We also note that we detect substantially more [N II] emission than can be seen in the images of S89 or the contour diagram of AP93. As with the previously discussed remnants, the majority of these new features are quite faint and are probably revealed here by the higher sensitivity of the narrow GFPI bandpass to low surface brightness emission. In addition, however, the data cube reveals more emission in the northeastern rim of the remnant, mostly near zero radial velocity, than is seen in the $H_\alpha$+[N II] image presented in Fig. 11 of S89; and this emission is spatially coincident with strong features seen in their [O III] image. Spectra extracted from our data cubes indicate that the total $H_\alpha$+[N II] detected fluxes from knots within the northeastern limb which do not appear in the $H_\alpha$+[N II] image of S89 are equivalent to the total detected fluxes from some of the strongest features located in the southwestern limb of the same image. This suggests that there has been recent evolution in the physical conditions of the remnant's northeastern rim, with features in this region growing stronger in $H_\alpha$+[N II] emission. It would appear to lend support to the proposal by S89 that variations in [N II] emission across the nebula represent different conditions in the shock-heated ejecta in each region, rather than variations in elemental abundances. Recent strengthening of [N II] in this limb might represent the beginning of interactions with circumstellar material in the northeastern polar region, similar to what is seen in the opposite, southwestern limb.

Also noteworthy is the slight "bulge" protruding from the south–southeastern portion of the remnant, visible in Figs. 6(a) and 6(b) and also frames 5–8 and 15 of Fig. 7. This feature is located between position angles 130° and 210° E of N, and spans radial velocities from $-500$ km s$^{-1}$ to $+700$ km s$^{-1}$. At its maximum outer extent, the bulge extends 5″–10″ farther outward from GK Per than the flattened limb regions described above. This larger radius could be due to a higher initial ejection velocity in this direction, less deceleration than has been experienced in other directions, or some combination of both. Duerbeck (1987a), S89 and AP93 have investigated the expansion of selected features in the remnant, primarily in the bright southwestern limb, and AP93

© American Astronomical Society • Provided by the NASA Astrophysics Data System

1995AJ....109.2635L



found evidence that at least some knots are expanding into regions where the ambient density is lower.

## 7. SUMMARY

In this paper we have presented observations and spatial models that demonstrate the tremendous potential Fabry–Perot imaging spectroscopy has for the study of nebular remnants from stellar explosions. The tunability of both the width and central wavelength of the etalon bandpass allows efficient scanning of the large-velocity dispersions intrinsic to these objects, and for identical sampling in velocity space among different emission lines. The combination of high spectral resolution and a wide field of view allows the observer to cover the entire surface of the remnant and distinguish overlapping but kinematically distinct structures on both large and small scales.

The observations of the Crab Nebula in [O III] λ5007 demonstrate that the high-helium torus first detected by Uomoto & MacAlpine (1987) is a thin, annular sheet-like structure, ~7 ly in diameter, ~0.25 ly thick, and ~1.9 ly in radial extent, fairly well centered on the pulsar and center of explosion. The intensity of the line emission varies markedly about its circumference, and the strongest region of [O III] emission is associated with one of the most helium-rich structures in the nebula. The data cubes provide more detail on the relationship between the remaining [O III]-bright filament loops, this torus, and the overall N–S bipolar asymmetry seen in the nebula. In general, the most intense [O III] emission originates from a 1.0–2.5 ly thick zone on the inner edge of the filamentary shell, surrounding the inner synchrotron cavity. Many short, finger-like radial extensions of [O III] emission protrude into the inner synchrotron region, as do several sheet-like extensions from the brightest filament loops; these features may be evidence of Rayleigh–Taylor instabilities in the filamentary ejecta. The highest radial velocity gas, both redshifted and blueshifted, is located in the northwestern region of the remnant. Holes in the distribution of the brightest filaments delineate an axis coincident with the major NW–SE axis of the remnant, and are also remarkably well aligned with activity in the synchrotron nebula near the pulsar. The data cube also reveals the spatial coincidence between the remarkable line of compact knots reported by MacAlpine *et al.* (1994) and a more highly redshifted filament, suggesting that these knots may also be the result of instabilities in the filament.

A scan of the FMKs in Cas A in [S II] λλ 6716, 6731 shows that this system can be grouped into four regions, distinguished by their spatial and kinematic properties. The northern arc is found to span the largest range of radial velocity ($\gtrsim$9500 km s$^{-1}$) and consists of two distinct rings of material. The larger, more redshifted ring appears to contain a large fraction of the [O III] strong knots, indicating an asymmetry in the abundance distribution or shock conditions associated with this structure. The region to the northeast can be divided into five substructures which, taken together, span ~7500 km s$^{-1}$ and surround the base of the jet. The southwestern arc and the irregular patches to the southeast span ~6500 and ~5000 km s$^{-1}$, respectively, and both show indications of further strengthening in their [S II] emissions. Asymmetries seen previously in the proper motions and distributions of the FMKs are matched by an overall inequality in the largest radial velocities detected in our spatially complete sampling; the most highly redshifted features in the northern arc have significantly larger space velocities ($\gtrsim$6900 km s$^{-1}$) than the space velocities of the most highly blueshifted features in the southeastern irregular emission (5100 km s$^{-1}$). The $H_\alpha$+[N II] λλ6548, 6583 scan of the QSFs in Cas A reveals several new flocculi and four regions of diffuse gas which have not been previously defined. Much of this diffuse gas has stronger [N II] than $H_\alpha$ emission, similar to most QSFs, and may be nitrogen-enriched gas shed from the progenitor star. The data also indicate that the QSFs and diffuse gas are distributed in a 12.4×6.1 ly elliptical region on the sky, extending well beyond the spherical distribution of FMKs in the southwest. This distribution may be indicative of asymmetries in the pre-supernova mass loss or in the interactions between the shock wave and the circumstellar material.

Observations of nova GK Per in $H_\alpha$+[N II] λλ 6548, 6583 provide a more complete picture of the remnant shell, and confirm the much greater strength of [N II] emission relative to $H_\alpha$. The spatial model shows that the northern, blueshifted "front" region and the eastern, low-radial-velocity "central" region are significantly lacking in [N II] emissions. In addition to the previously detected box-like asymmetry of the shell, a small bulge to the south–southeast is also present. Comparisons with previous imaging studies suggest that [N II] emission from the northeastern limb has strengthened in recent years, lending support to the hypothesis that differences between the [N II] and [O III] line ratios across the face of the remnant are due to varying shock and excitation conditions, rather than abundance differences.

We would like to thank J. N. Bregman for access to the Stardent Graphics Supercomputer used to generate the three-dimensional displays presented in this paper, and K. Gebhardt for providing and helping adapt his simulation program for use in determining our uncertainties. This work was partially supported through a Rackham School of Graduate Studies Dissertation Grant to S.S.L.

## REFERENCES

Anupama, G. C., & Prabhu, T. P. 1993, MNRAS, 263, 335 (AP93)
Aschenbach, B., & Brinkmann, W. 1975, A&A, 41, 147
Atherton, P. D., Reay, N. K., Ring, J., & Hicks, T. R. 1981, Opt. Engineering, 20, 806
Baade, W., & Minkowski, R. 1954, ApJ, 119, 206
Bandiera, R., Pacini, F., & Salvati, M. 1983, A&A, 126, 7
Beers, T. C., Flynn, K., & Gebhardt, K. 1990, AJ, 100, 32
Bland, J., & Tully, R. B. 1989, AJ, 98, 723
Bode, M. F., Duerbeck, H. W., Seitter, W. C., Albinson, J. S., & Evans, A. 1988, in A Decade of UV Astronomy with the IUE Satellite, edited by E.

© American Astronomical Society • Provided by the NASA Astrophysics Data System

1995AJ....109.2635L



J. Rolfe (European Space Agency, Paris), p. 183
Bode, M. F., Seaquist, E. R., & Evans, A. 1987a, MNRAS, 228, 217
Bode, M. F., Seaquist, E. R., Frail, D. A., Roberts, J. A., Whittet, D. C. B., Evans, A., & Albinson, J. S. 1987b, Nature, 329, 519
Brinkmann, W., Aschenbach, B., & Langmeier, A. 1985, Nature, 313, 662
Caulet, A., *et al.* 1992, ApJ, 388, 301
Chevalier, R. A. 1977, ARA&A, 15, 175
Chevalier, R. A., & Gull, T. R. 1975, ApJ, 200, 399
Clark, D. H., Murdin, P., Wood, R., Gilmozzi, R., Danziger, J., & Furr, A. W. 1983, MNRAS, 204, 415
Couderc, P. 1939, Ann. d'Astrophys., 2, 271
Cox, D. P., & Raymond, J. C. 1985, ApJ, 298, 651
Curtis, H. N. 1919, Lick Obs. Bull., 10, 35
Crampton, D, Cowley, A. P., & Fisher, W. A. 1986, ApJ, 300, 788
Davidson, K., & Fesen, R. A. 1985, ARA&A, 23, 119
Dopita, M. A., Binnette, L., D'Odorico, S., & Benvenuti, P. 1984, ApJ, 276, 653
Duerbeck, H. W. 1987a, Ap&SS, 131, 461
Duerbeck, H. W. 1987b, in A Reference Catalogue and Atlas of Galactic Novae (Reidel, Dordrecht), p. 89
Duerbeck, H. W., & Seitter, W. C. 1987, Ap&SS, 131, 467
Fesen, R. A., & Becker, R. H. 1991, ApJ, 371, 621 (FB91)
Fesen, R. A., & Blair, W. P. 1990, ApJ, 351, L45
Fesen, R. A., Becker, R. H., & Blair, W. P. 1987, ApJ, 313, 378 (FBB)
Fesen, R. A., Becker, R. H., & Goodrich, R. W. 1988, ApJ, 329, L89 (FBG)
Fesen, R. A., & Kirshner, R. P. 1982, ApJ, 258, 1 (FK82)
Fesen, R. A., Martin, C. L., & Shull, J. M. 1992, ApJ, 399, 599
Fesen, R. A., & Staker, B. 1993, MNRAS, 263, 69
Gebhardt, K., Pryor, C., Williams, T. B., & Hesser, J. E. 1994, AJ, 107, 2067
Henry, R. B. C., MacAlpine, G. M., & Kirshner, R. P. 1984, ApJ, 278, 619 (HMK)
Hester, J. J., Scowen, P. A., Gallagher, J., & the WFPC-2 IDT. 1994, BAAS, 26, 951
Kamper, K. W., & van den Bergh, S. 1976, ApJS, 32, 351 (KB76)
Kirshner, R. P., & Chevalier, R. A. 1977, ApJ, 218, 142
Küstner, F. 1921, in Jubiläumsnummer zum hundertjährigen bestehen Astronomische Nachrichten, edited by H. A. Kobold (C. Schaidt, G. Oheim, Kiel), p. 18
MacAlpine, G. M., & Lawrence, S. S. 1995, in preparation
MacAlpine, G. M., Lawrence, S. S., Brown, B. A., Uomoto, A., Woodgate, B. E., Brown, L. W., Oliversen, R. J., Lowenthal, J. D., & Liu, C. 1994, ApJ, 432, L131 (M94)
MacAlpine, G. M., McGaugh, S. S., Mazzarella, J. M., & Uomoto A. 1989, ApJ, 342, 364 (M89)
Massey, P., Strobel, K., Barnes, J., & Anderson, E. 1988, ApJ, 328, 315
McKee, C. F., & Cowie, L. L. 1975, ApJ, 195, 715
McLaughlin, D. B. 1960, in Stars and Stellar Systems, Vol. 6, Stellar Atmospheres, edited by J. L. Greenstein (University of Chicago Press, Chicago), p. 585
Michel, F. C., Scowen, P. A., Dufour, R. J., & Hester, J. J. 1991, ApJ, 368, 463
Miller, J. S. 1978, ApJ, 220, 490
Oort, J. H. 1951, in Problems of Cosmical Aerodynamics, edited by J. Burgess (Central Air Documents, Dayton, Ohio), p. 118
Osterbrock, D. E. 1989, in Astrophysics of Gaseous Nebulae and Active Galactic Nuclei (University Science Books, Mill Valley, CA)
Peimbert, M., & van den Bergh, S. 1971, ApJ, 167, 223
Reed, J. E., Fabian, A. C., & Winkler, P. F. 1989, in Supernovae, edited by S. E. Woosley (Springer, New York), p. 649
Reed, J. E., Fabian, A. C., & Winkler, P. F. 1991, BAAS, 23, 826
Reynolds, S. P., & Chevalier, R. A. 1984, ApJ, 281, L33
Sabbadin, F., & Bianchini, A. 1983, A&AS, 54, 393
Scargle, J. D. 1969, ApJ, 156, 401
Schaefer, B. 1988, ApJ, 327, 347
Scowen, P. A., Hester, J. J., Gallagher, J., Lynds, R., O'Neil, Jr., E. J., Currie, D. G., the WF/PC IDT, and the WFPC-2 IDT. 1994, BAAS, 26, 951
Seaquist, E. R., Bode, M. F., Frail, D. A., Roberts, J. A., Evans, A., & Albinson, J. S. 1989, AJ, 344, 805 (S89)
Seitter, W. C., & Duerbeck, H. W. 1987, in RS Ophiuchi (1985) and the Recurrent Nova Phenomenon, edited by M. F. Bode (VNU Science Press, Utrecht), p. 71
Swope, H. 1940, Harvard Bull. No. 913, 11
Trimble, V. 1968, AJ, 73, 535 (T68)
Trimble, V. 1970, AJ, 75, 926 (T70)
Trimble, V. 1973, PASP, 85, 579
Uomoto, A., & MacAlpine, G. M. 1987, AJ, 93, 1511
van den Bergh, S. 1970, ApJ, 160, L27
van den Bergh, S. 1971a, ApJ, 165, 259
van den Bergh, S. 1971b, ApJ, 165, 457
van den Bergh, S. 1977, PASP, 89, 637
van den Bergh, S., & Dodd, W. W. 1970, ApJ, 162, 485
van den Bergh, S., & Kamper, K. W. 1983, ApJ, 268, 129 (BK83)
van den Bergh, S., & Kamper, K. W. 1985, ApJ, 293, 537 (BK85)
van den Bergh, S., & Pritchet, C. J. 1986, Nature, 321, 46
Wyckoff, S., & Murray, C. A. 1977, MNRAS, 180, 717 (WM)
Wyckoff, S., Wehinger, P. A., Fosbury, R. A. E., & Mullan, D. 1976, ApJ, 206, 254

© American Astronomical Society • Provided by the NASA Astrophysics Data System

1995AJ....109.2635L



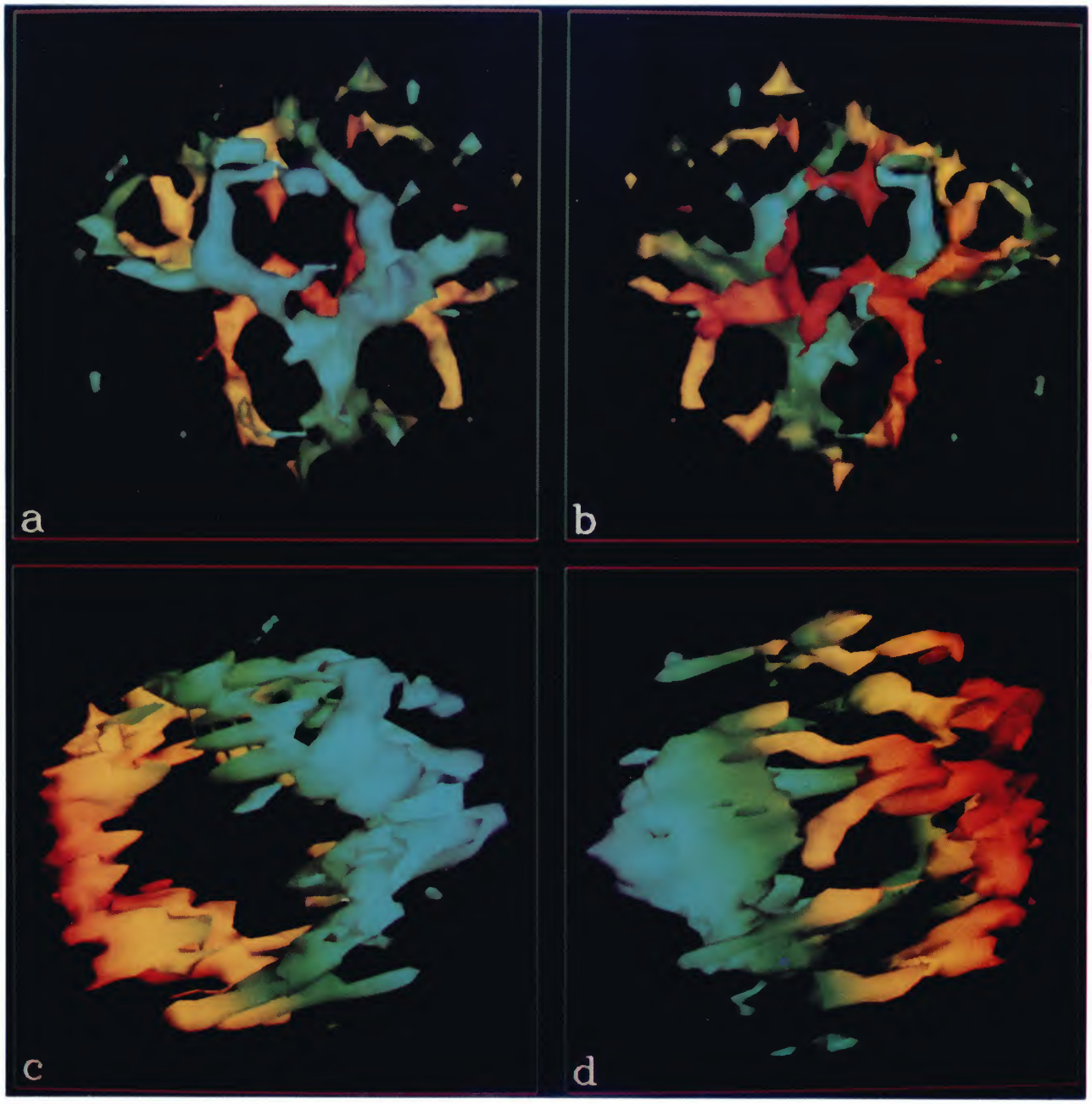


FIG. 1. Views of the [O III] spatial model of the Crab Nebula. Color coding represents radial velocity, ranging from $-1500$ km s$^{-1}$ (deep blue) to $+1400$ km s$^{-1}$ (deep red). (a) displays the model as seen from the Earth. North is up, east is to the left. (b) presents the model from a vantage point 180° from that of (a), showing the back of the nebula. (c) views the model from a line of sight 60° east from a line of sight to the Earth, and 30° south of the E–W plane. (d) illustrates a line of sight 120° west of a line of sight to the Earth, and 30° south of the E–W plane.

Lawrence *et al.* (see page 2640)

© American Astronomical Society • Provided by the NASA Astrophysics Data System

1995AJ....109.2635L



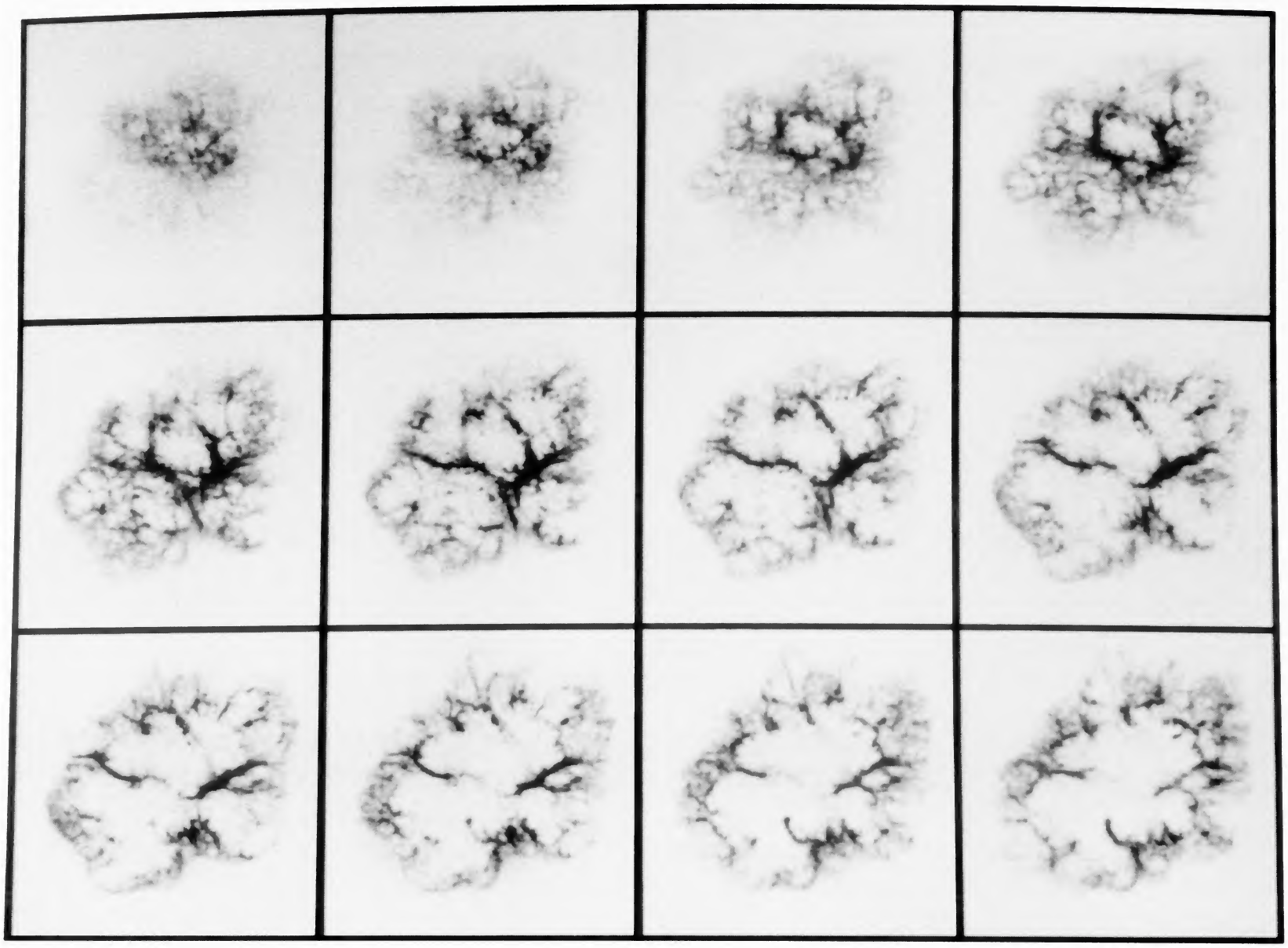

FIG. 2. (a) A mosaic of frames displaying a representative section of the data interpolated $I(\alpha,\delta,\lambda)$ data cube of the Crab Nebula in [O III] λ5007 emission. Each frame is a 5.3 Å FWHM image of the Crab, centered on wavelengths listed in Table 3. North is up and east is to the left. Frames are ordered in increasing wavelength from left to right, beginning in the upper left. Velocities in the observer's rest frame are −1435, −1300, −1170, −1045, −915, −780, −655, −525, −390, −260, −135, and −5 km s$^{-1}$, respectively. (b) Velocities in the observer's rest frame are +130, +255, +385, +520, +650, +775, +910, +1040, +1165, +1295, and +1430 km s$^{-1}$, respectively, for frames 1 through 11. Frame 12 contains a stacked image formed by the addition of all images within the irregular $I(\alpha,\delta,\lambda)$ data cube.



 © American Astronomical Society • Provided by the NASA Astrophysics Data System

1995AJ....109.2635L

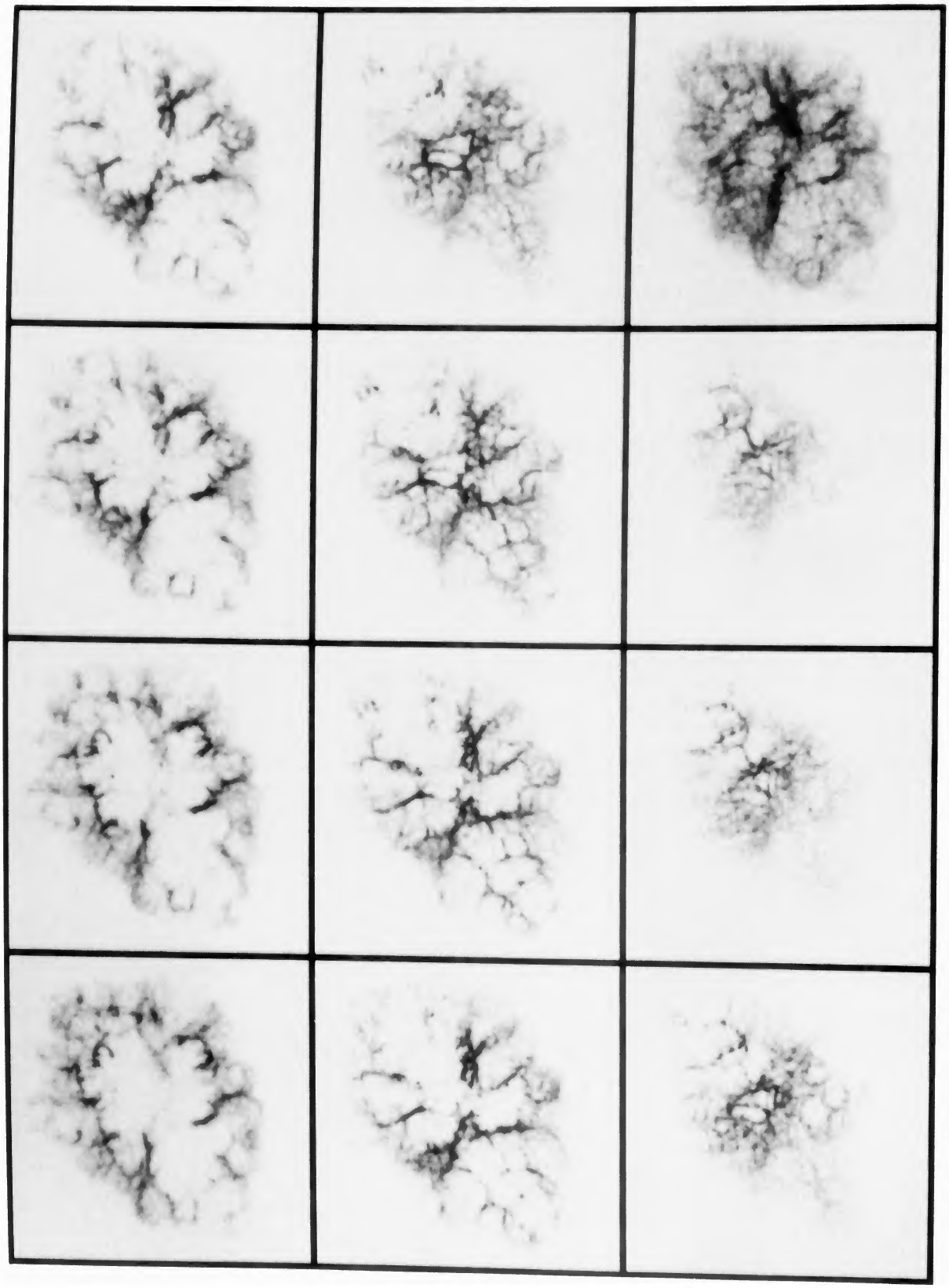

FIG. 2. (continued)

Lawrence *et al.* (see page 2640)

© American Astronomical Society • Provided by the NASA Astrophysics Data System

1995AJ....109.2635L

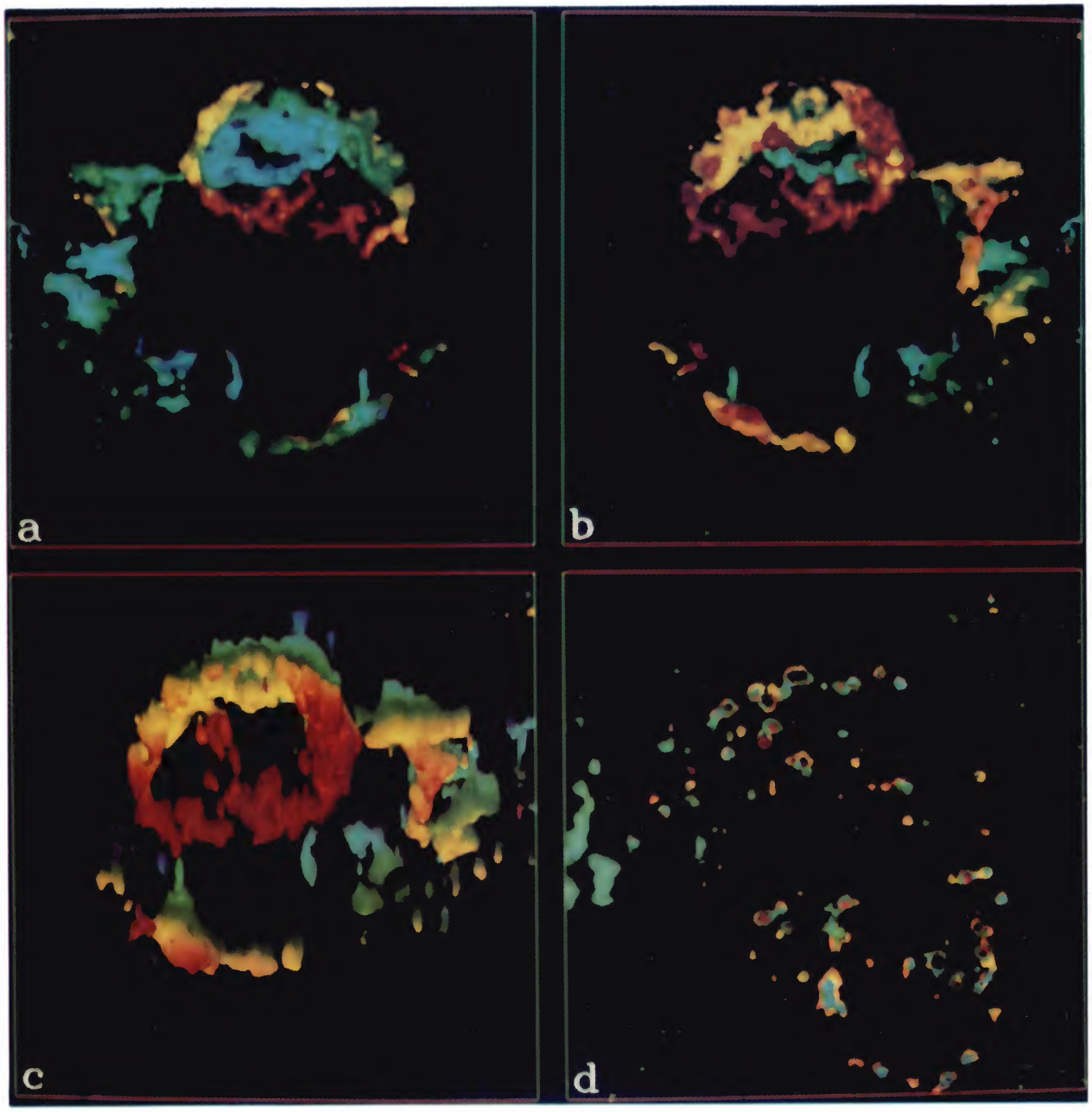


FIG. 3. Views of the spatial models of Cas A. (a)–(c) show the fast-moving knots in [S II] emission. Color coding is representative of radial velocity, ranging from −5100 (deep blue) to +6100 km $s^{-1}$ (deep red). (a) displays the model as seen from the Earth. North is up, east is to the left. (b) presents the model from a vantage point 180° from that of (a), showing the back of the FMK system. (c) contains a view of the model from a line of sight 20° north from that of (b), showing the nebula from behind and slightly above. (d) shows the quasi-stationary flocculi in $H_\alpha$+[N II] emission, as seen from the Earth. Color coding represents wavelength, ranging from 6548 (deep blue) to 6600 Å (deep red).

Lawrence *et al.* (see page 2644)

 © American Astronomical Society • Provided by the NASA Astrophysics Data System

1995AJ....109.2635L

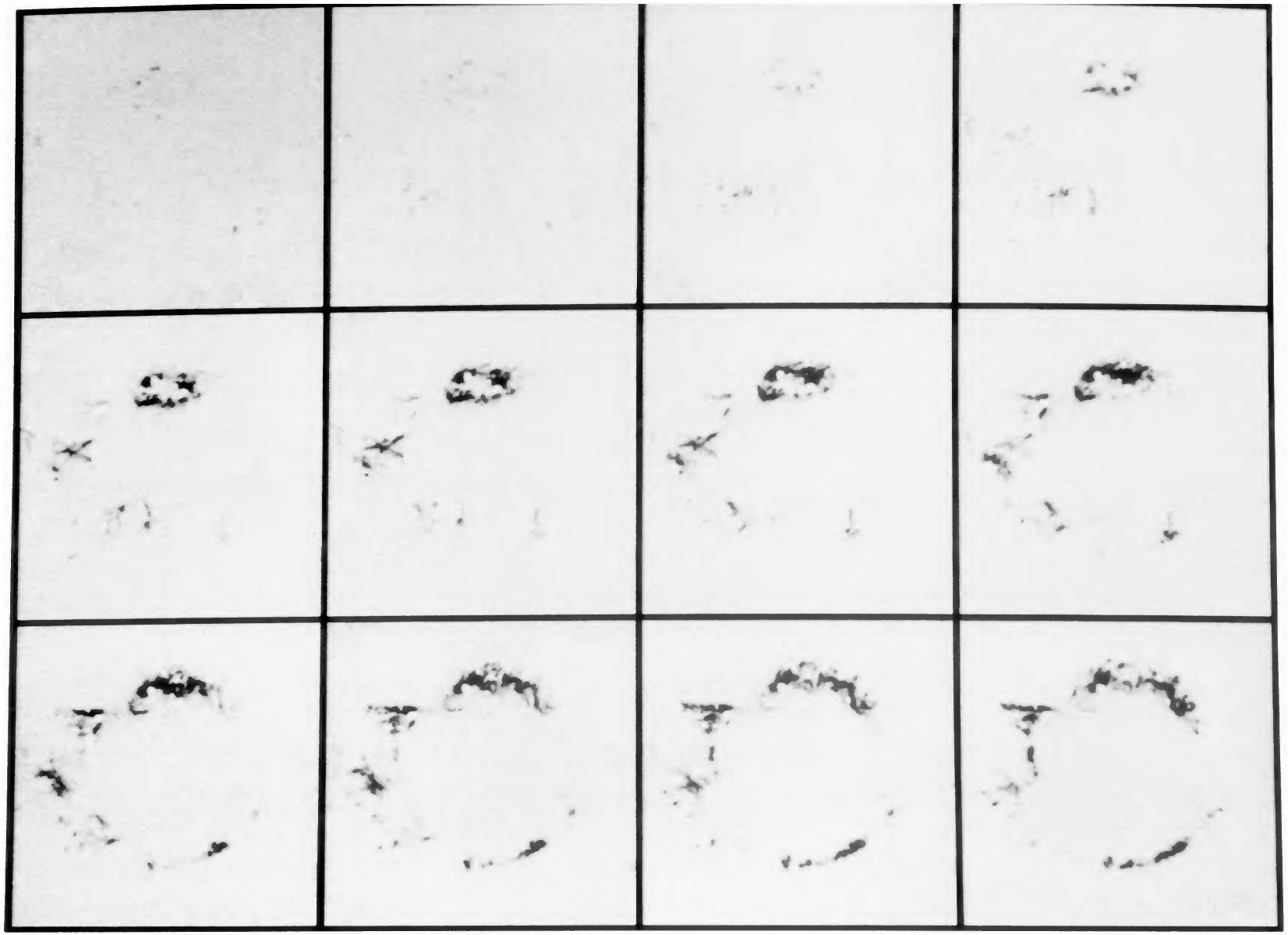

FIG. 4. (a) A mosaic of frames representing the interpolated $I(\alpha,\delta,\lambda)$ data cube of the fast-moving knots of Cas A in [S II] λλ 6716, 6731 emission. Each frame is a 14.4 Å FWHM image of the remnant, centered on wavelengths listed in Table 3. North is up and east is to the left. Frames are ordered in increasing wavelength from left to right, beginning in the upper left. Velocities in the observer's rest frame are −5035, −4500, −3965, −3430, −2895, −2360, −1825, −1285, −750, −215, +320, and +855 km s$^{-1}$, respectively. (b) Velocities in the observer's rest frame are +1390, +1925, +2460, +2995, +3530, +4070, +4605, +5140, and +5675 km s$^{-1}$, respectively, for frames 1 through 9. Frames 10 and 11 have been left blank and frame 12 contains a stacked image formed by the addition of all images within the irregular $I(\alpha,\delta,\lambda)$ data cube.



© American Astronomical Society • Provided by the NASA Astrophysics Data System

1995AJ....109.2635L

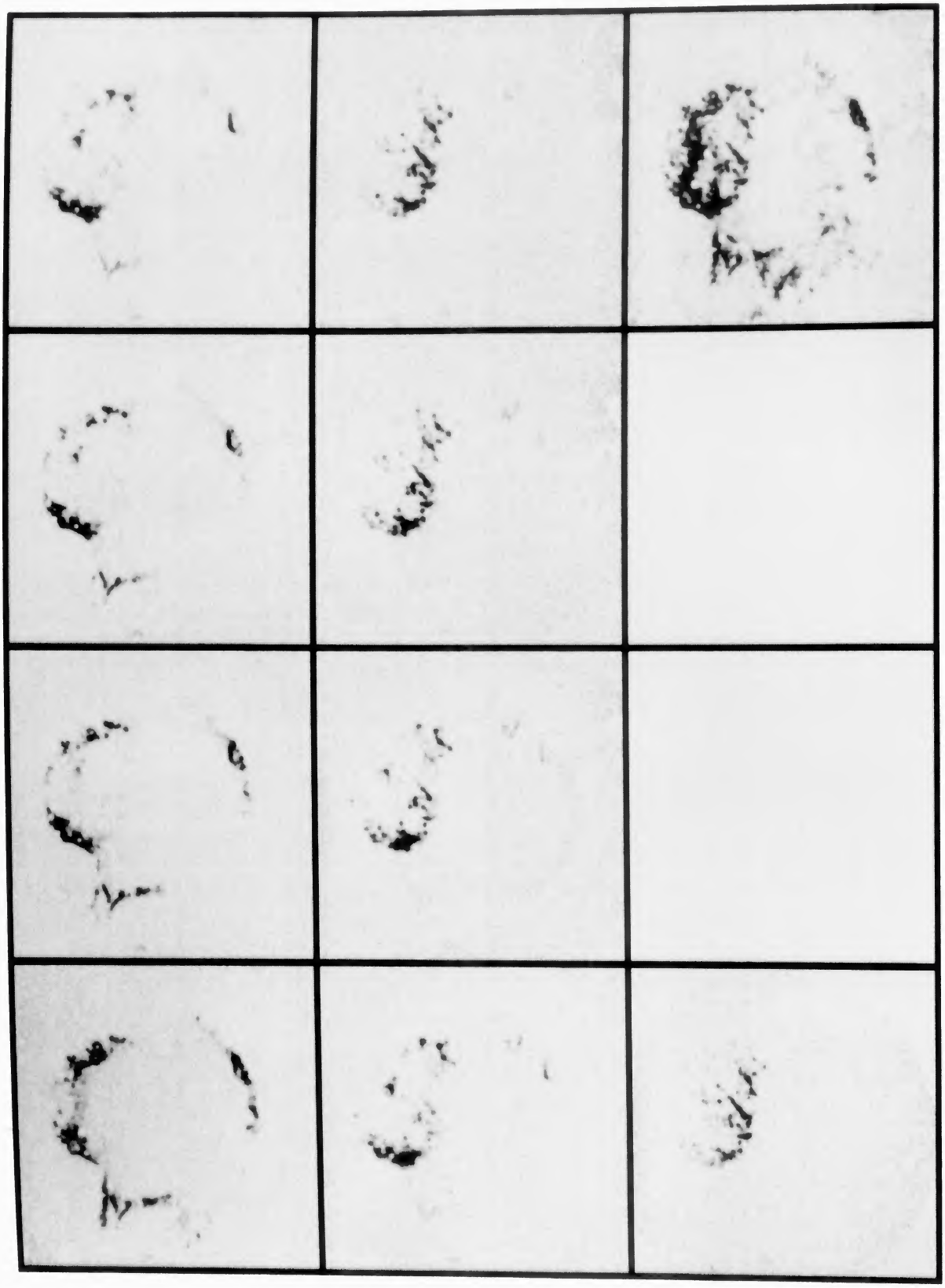

FIG. 4. (continued)

Lawrence *et al.* (see page 2644)

 © American Astronomical Society • Provided by the NASA Astrophysics Data System

1995AJ....109.2635L

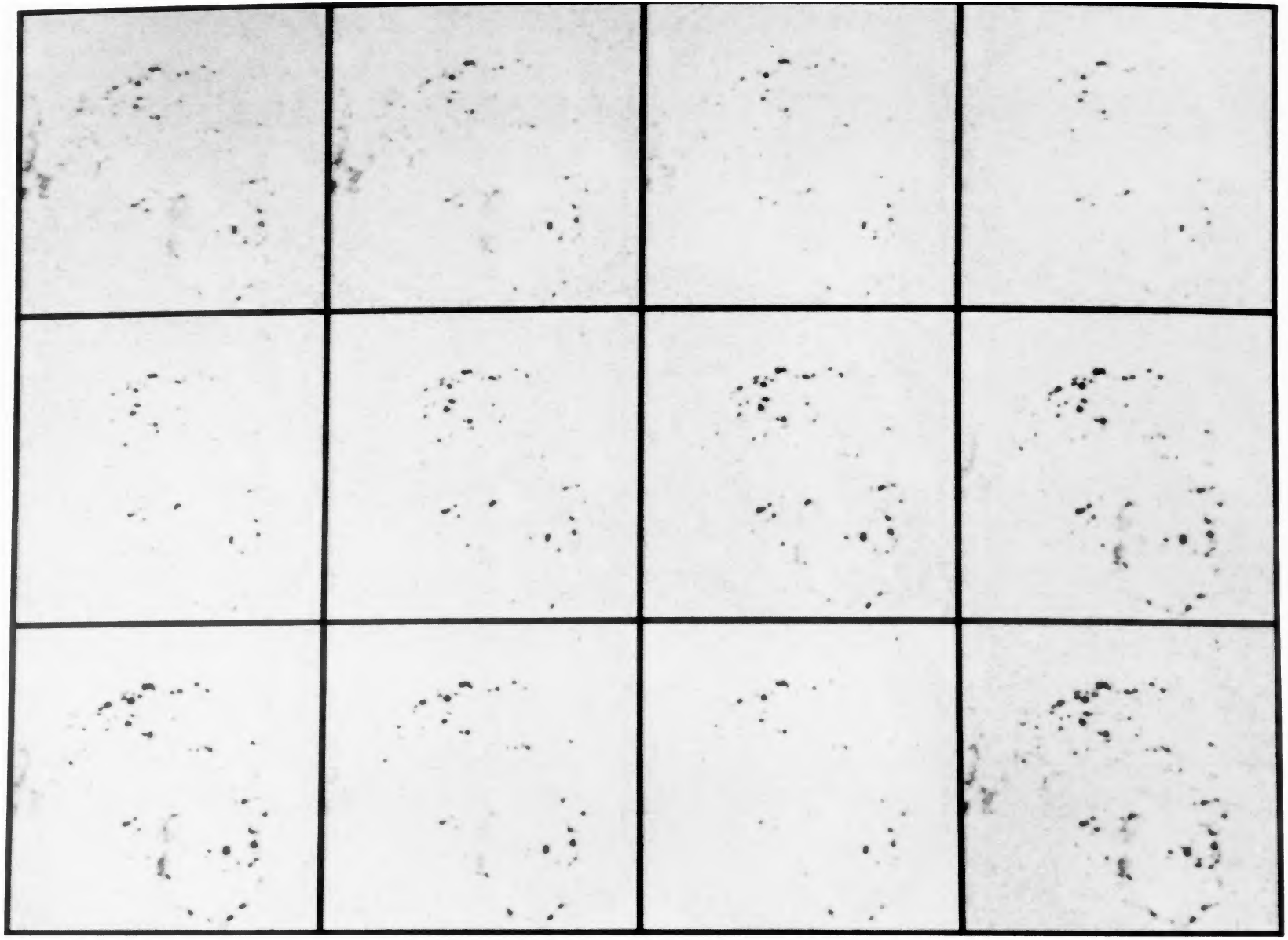

FIG. 5. A mosaic of frames displaying a representative portion of the interpolated $I(\alpha,\delta,\lambda)$ data cube of the quasi-stationary flocculi of Cas A in $H_\alpha$+[N II] λλ 6548, 6583 emission. Each frame is a 5.3 Å FWHM image of the remnant, centered on wavelengths listed in Table 3. North is up and east is to the left. Frames are ordered in increasing wavelength from left to right, beginning in the upper left. Velocities relative to $H_\alpha$ in the observer's rest frame are −100, +30, +160, +290, +420, +550, +680, +810, +940, +1070, and +1200 km $s^{-1}$, respectively, for frames 1 through 11. Frame 12 contains a stacked image formed by the addition of all images within the irregular $I(\alpha,\delta,\lambda)$ data cube.



© American Astronomical Society • Provided by the NASA Astrophysics Data System

1995AJ....109.2635L

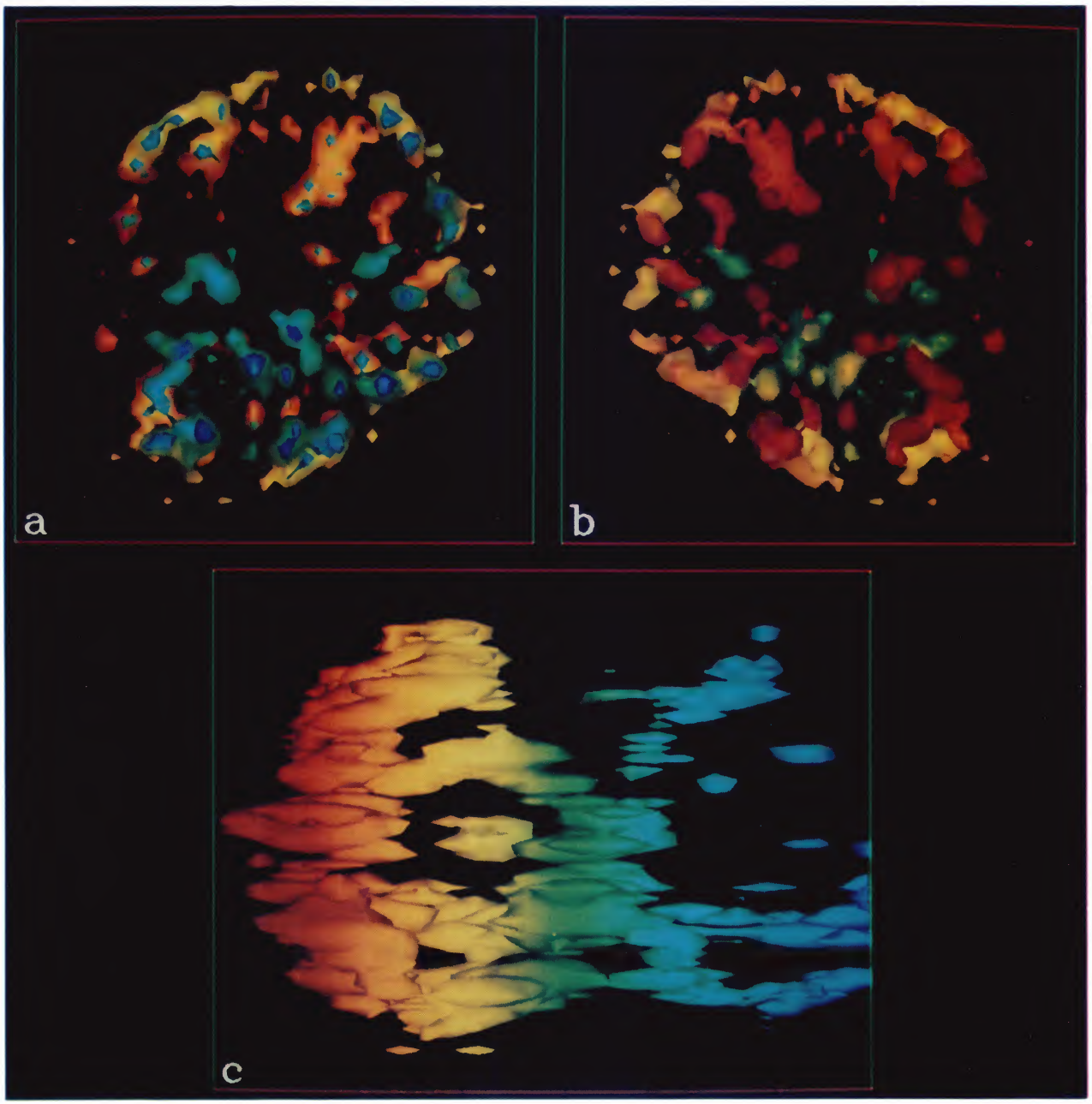


FIG. 6. Views of the spatial model of nova GK Per in $H_\alpha$+[N II] emission. Color coding is representative of wavelength, ranging from 6536 (deep blue) to 6612 Å (deep red). (a) displays the model as seen from along the line of sight to the Earth. North is up, east is to the left. (b) presents the model from a vantage point 180° from that of (a), showing the back of the remnant. (c) contains a view of the model from a line of sight 90° west from a line of sight to the Earth, and displays the relative intensities of features in the three emission lines.

Lawrence *et al.* (see page 2648)

 © American Astronomical Society • Provided by the NASA Astrophysics Data System

1995AJ....109.2635L



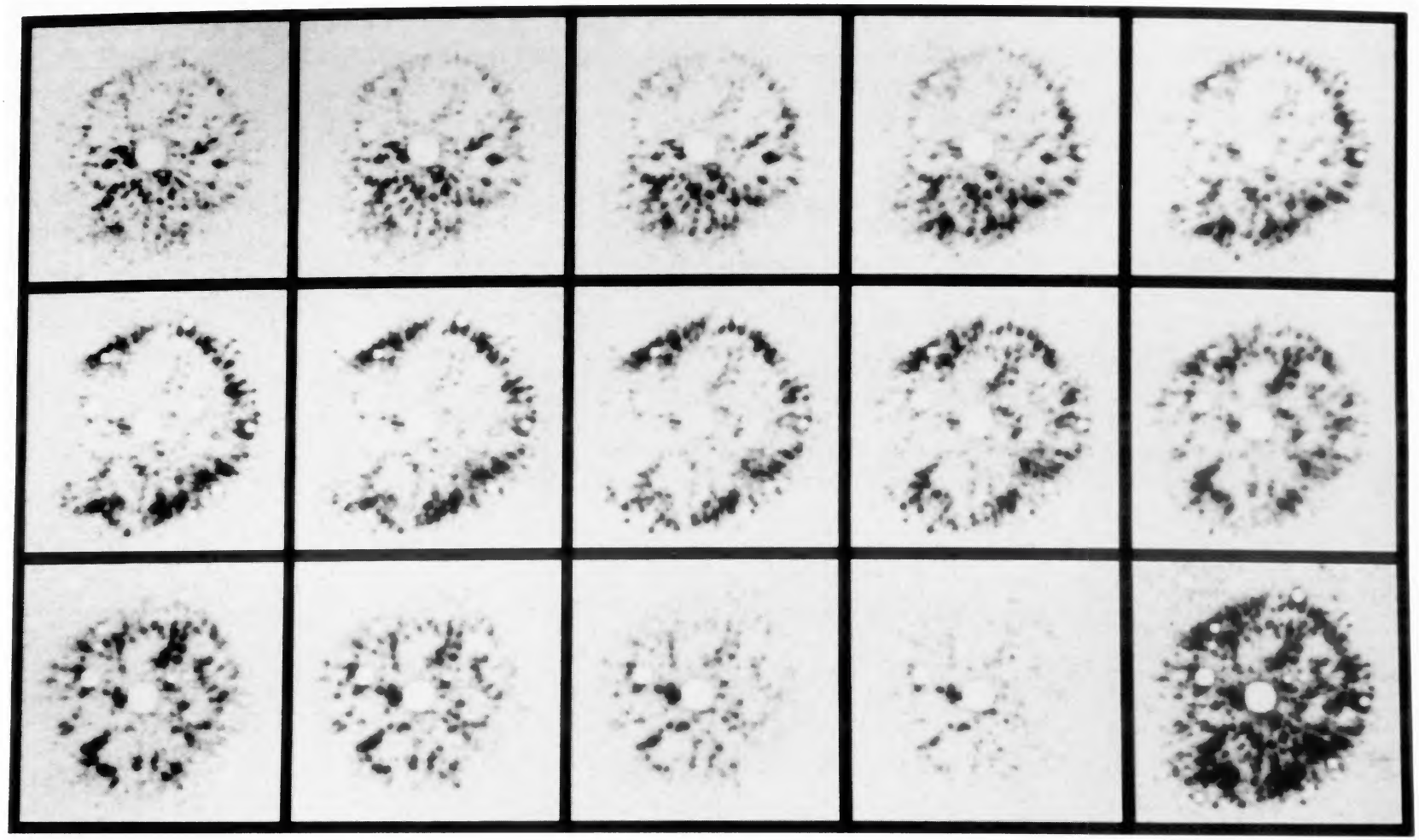

FIG. 7. A mosaic of frames displaying a representative portion of the interpolated $I(\alpha,\delta,\lambda)$ data cube of the GK Per nova remnant in $H_\alpha$+[N II] λλ 6548, 6583 emission. Each frame is a 5.3 Å FWHM image of the remnant, centered on wavelengths listed in Table 3. North is up and east is to the left. Frames are ordered in increasing wavelength from left to right, beginning in the upper left. Velocities relative to [N II] λ 6583 in the observer's rest frame are −840, −700, −560, −420, −280, −140, 0, +140, +280, +420, +560, +700, +840, and +980 km $s^{-1}$, respectively, for frames 1 through 14. Frame 15 contains a stacked image formed by the addition of all images within the irregular $I(\alpha,\delta,\lambda)$ data cube.

Lawrence *et al.* (see page 2649)

© American Astronomical Society • Provided by the NASA Astrophysics Data System